

Utah State University

DigitalCommons@USU

---

All Graduate Theses and Dissertations

Graduate Studies

---

5-2021

## Application of Computational Fluid Dynamics to Determine Gas Expansion Factors of Differential Pressure Flow Meters

Patrick L. Campana  
*Utah State University*

Follow this and additional works at: <https://digitalcommons.usu.edu/etd>



Part of the [Civil and Environmental Engineering Commons](#)

---

### Recommended Citation

Campana, Patrick L., "Application of Computational Fluid Dynamics to Determine Gas Expansion Factors of Differential Pressure Flow Meters" (2021). *All Graduate Theses and Dissertations*. 8074.

<https://digitalcommons.usu.edu/etd/8074>

This Thesis is brought to you for free and open access by the Graduate Studies at DigitalCommons@USU. It has been accepted for inclusion in All Graduate Theses and Dissertations by an authorized administrator of DigitalCommons@USU. For more information, please contact [digitalcommons@usu.edu](mailto:digitalcommons@usu.edu).



APPLICATION OF COMPUTATIONAL FLUID DYNAMICS TO DETERMINE GAS  
EXPANSION FACTORS OF DIFFERENTIAL PRESSURE FLOW METERS

by

Patrick L. Campana

A thesis submitted in partial fulfillment  
of the requirements for the degree

of

MASTER OF SCIENCE

in

Civil and Environmental Engineering

Approved:

---

Zachary B. Sharp, Ph. D., P.E.  
Major Professor

---

Michael C. Johnson, Ph.D., P.E.  
Committee Member

---

Som Dutta, Ph. D.  
Committee Member

---

D. Richard Cutler, Ph.D.  
Interim Vice Provost  
of Graduate Studies

UTAH STATE UNIVERSITY  
Logan, Utah

2021

Copyright © Patrick L. Campana 2021

All Rights Reserved

## ABSTRACT

Application of Computation Fluid Dynamics to determine gas expansion factors of  
differential Pressure Flow Meters

by

Patrick L. Campana, Master of Science

Utah State University, 2021

Major Professor: Dr. Zachary B. Sharp  
Department: Civil and Environmental Engineering

The purpose of this research was to investigate if computational fluid dynamics could be used to predict differential pressure flow meter gas expansion factor values with sufficient accuracy to use the values for the regression of accurate empirical gas expansion equations for a variety of differential pressure flow meter geometries. Simulations of incompressible and compressible flows through Classical Venturis, Stand Concentric orifice plates, and wedge meters were conducted to characterize the performance of these flow meters over a variety of flow rates and pressure differentials. Incompressible flows were modeled using the fluid properties of water. Compressible flows were modeled using the assumption of a perfect gas with the fluid properties of dry air. Compressible effects were modeled using the ideal gas law.

Classical Venturi and Standard Concentric orifice plate gas expansion factors produced from computational fluid dynamics simulations matched their respective International Organization for Standardization endorsed theoretical or empirical gas

expansion factor values with remarkable accuracy. This indicates computational fluid dynamics is an appropriate tool for determining differential pressure flow meter gas expansion factor values. In addition, wedge meter gas expansion factor values were determined using the same modeling approach. The wedge meter gas expansion factors produced using computational fluid dynamics were reasonable for a variety of bore sizes and pressure differentials.

(93 pages)

## PUBLIC ABSTRACT

### Application of Computation Fluid Dynamics to determine gas expansion factors of differential Pressure Flow Meters

Patrick L. Campana

The purpose of this research was to investigate if computer simulations could be used to accurately predict gas expansion in differential pressure flow meters. Differential pressure flow meters are used to measure the flow rate of pressurized liquids and gases through pipes. Computer simulations of liquid and gas flows were conducted for three distinct differential pressure flow meter geometries: Classical Venturis, Stand Concentric orifice plates, and wedge meters.

Gas flows were modeled as dry air using the assumption of a perfect gas. Expansion effects were modeled using the ideal gas law. Computer simulations of Classical Venturi and Standard Concentric orifice plates predicted gas expansion that matched existing laboratory data with remarkable accuracy. This indicates the computer simulation method, known as computational fluid dynamics, is an appropriate tool for determining gas expansion in differential pressure flow meters. Computer simulations of wedge meters were then conducted using the same modeling approach and produced reasonable gas expansion factor values.

## ACKNOWLEDGMENTS

This study would never have come to fruition without the infinite patience and wisdom of Dr. Zac Sharp. Zac, thank you for the invaluable CFD instruction, encouraging me to continue working on this project despite the many setbacks and difficulties I faced, and allowing me to operate with an incredible degree of autonomy. It has been an absolute pleasure to work with you. Also special thanks to Dr. Michael Johnson and Dr. Som Dutta for their valuable feedback and instruction. Finally, thank you to the love of my life, Brianna Allen, for the endless support you provided and your patience during the many days and nights we spent apart during this process.

Patrick L. Campana

## CONTENTS

	Page
Abstract.....	iii
Public Abstract.....	v
Acknowledgments.....	vi
List of Tables .....	ix
List of Figures.....	xi
List of Symbols.....	xiv
Chapter I Introduction.....	1
Chapter II Theoretical Background .....	3
Chapter III Literature Review .....	8
Chapter IV Research Objectives.....	12
Chapter V Simulation Setup .....	13
Established Method to Determine Compressible Flow Discharge Coefficients in a Laboratory Setting .....	13
Physics Models .....	14
Determination of Simulation Parameters and Flow Conditions .....	15
Incompressible Flow.....	16
Compressible Flow.....	16
Calculation or Selection of Simulation Boundary Values .....	18
Velocity Inlet Boundary.....	18
Pressure Outlet Boundaries.....	19
Wall Boundaries.....	19
DPFM Dimensions and Mesh Generation .....	20
Classical Venturi Meter Dimensions .....	20
Classical Venturi Meshing.....	21
Standard Concentric Orifice Plate Meter Dimensions.....	22
Standard Concentric Orifice Plate Meter Meshing .....	23

Wedge Meter Dimensions.....	24
Wedge Meter Meshing.....	25
Simulation Parameters of Interest and Calculation of $\beta_{\text{actual}}$ , $Re_{\text{actual}}$ , $C_d$ , and $\varepsilon$ ....	26
Gas Expansion Factor Calculation Method .....	28
Mesh Independence and Acceptable Convergence Criteria .....	29
Chapter VI Results and Discussion.....	30
Classical Venturi Meter .....	30
Classical Venturi Incompressible Flow Simulations. ....	31
Classical Venturi Compressible Flow Simulations.....	35
Standard Concentric Orifice Plate .....	40
Standard Concentric Orifice Plate Incompressible Flow Simulations.....	41
Standard Concentric Orifice Plate Compressible Flow Simulations. ....	46
Wedge Meter.....	51
Wedge Meter Incompressible Flow Simulations.....	52
Wedge Meter Compressible Flow Simulations. ....	55
Compressible Flow Visualizations .....	59
Gas Expansion Factor to Mach Number Relationship.....	64
Chapter VII Conclusion .....	66
Future Research .....	67
References.....	69
Appendix.....	74
Grid Convergence Index Results .....	75

## LIST OF TABLES

	Page
Table 1. STAR-CCM+ Physics Models .....	15
Table 2. Classical Venturi Dimensions.....	21
Table 3. Standard Concentric Orifice Plate Dimensions .....	23
Table 4. Wedge Meter Dimensions .....	25
Table 5. Incompressible Flow Discharge Coefficient Values for 0.4 $\beta$ Classical Venturi Determined Using Realizable K-Epsilon Two-Layer Turbulence Model.....	31
Table 6 Incompressible Flow Discharge Coefficient Values for 0.4 $\beta$ Classical Venturi Determined Using Standard Spalart-Allmaras Turbulence Model.....	31
Table 7. Incompressible Flow Discharge Coefficient Values for 0.4 $\beta$ Classical Venturi Determined Using SST(Menter) K-Omega Turbulence Model .....	32
Table 8. Incompressible Flow Discharge Coefficient Values for 0.4 $\beta$ Classical Venturi Determined Using Reynolds Stress Turbulence with Elliptic Blending Turbulence Model.....	32
Table 9. Incompressible Flow Discharge Coefficient Values for 0.5 $\beta$ Classical Venturi .....	32
Table 10. Incompressible Flow Discharge Coefficient Values for 0.6 $\beta$ Classical Venturi .....	32
Table 11. Gas Expansion Factors for 0.4 $\beta$ Classical Venturi Determined Using Realizable K-Epsilon Two-Layer Turbulence Model.....	36
Table 12. Gas Expansion Factors for 0.4 $\beta$ Classical Venturi Determined Using Standard Spalart-Allmaras Turbulence Model .....	36
Table 13. Gas Expansion Factors for 0.4 $\beta$ Classical Venturi Determined Using SST(Menter) K-Omega Turbulence Model .....	36
Table 14. Gas Expansion Factors for 0.4 $\beta$ Classical Venturi Determined Using Reynolds Stress Turbulence with Elliptic Blending Turbulence Model .....	36
Table 15. Gas Expansion Factors for 0.5 $\beta$ Classical Venturi .....	36

Table 16. Gas Expansion Factors for 0.6 $\beta$ Classical Venturi .....	37
Table 17. Incompressible Flow Discharge Coefficients for 0.4 $\beta$ Standard Concentric Orifice Plate.....	41
Table 18. Incompressible Flow Discharge Coefficients for 0.5 $\beta$ Standard Concentric Orifice Plate.....	42
Table 19. Incompressible Flow Discharge Coefficients for 0.6 $\beta$ Standard Concentric Orifice Plate.....	42
Table 20. Gas Expansion Factors for 0.4 $\beta$ Standard Concentric Orifice Plate.....	47
Table 21. Gas Expansion Factors for 0.5 $\beta$ Standard Concentric Orifice Plate.....	47
Table 22. Gas Expansion Factors for 0.6 $\beta$ Standard Concentric Orifice Plate.....	48
Table 23. Incompressible Flow Discharge Coefficient Values for 0.3789 $\beta$ Wedge Meter.....	52
Table 24. Incompressible Flow Discharge Coefficient Values for 0.5019 $\beta$ Wedge Meter.....	52
Table 25. Incompressible Flow Discharge Coefficient Values for 0.6107 $\beta$ Wedge Meter.....	53
Table 26. Gas Expansion Factors for 0.3789 $\beta$ Wedge Meter .....	55
Table 27. Gas Expansion Factors for 0.5019 $\beta$ Wedge Meter .....	55
Table 28. Gas Expansion Factors for 0.6107 $\beta$ Wedge Meter .....	56

## LIST OF FIGURES

	Page
Figure 1. Control Volume.....	4
Figure 2. Absolute Viscosity of Air at Different Static Pressures .....	18
Figure 3. Classical Venturi with Sharp Transitions .....	21
Figure 4. Classical Venturi 0.4 $\beta$ Half Profile .....	22
Figure 5. Classical Venturi Mesh.....	22
Figure 6. Standard Concentric Orifice Plate Profile.....	23
Figure 7. Cross Sectional View of a Standard Concentric Orifice Plate's Tip Mesh.....	24
Figure 8. Wedge Meter Side View .....	25
Figure 9. Cross Section of Wedge Meter Wedge Apex Mesh.....	26
Figure 10. Cross section of 0.3789 $\beta$ Wedge Meter Mesh.....	26
Figure 11. Incompressible Flow Discharge Coefficient Values and Trendline Equations for 0.4 $\beta$ Classical Venturi .....	33
Figure 12. Incompressible Flow Discharge Coefficient Values and Trendline Equation for 0.5 $\beta$ Classical Venturi.....	34
Figure 13. Incompressible Flow Discharge Coefficient Values and Trendline Equation for 0.5 $\beta$ Classical Venturi.....	34
Figure 14. Gas Expansion Factors for 0.4 $\beta$ Classical Venturi Determined Using Various Turbulence Models .....	37
Figure 15. Gas Expansion Factors for 0.4 $\beta$ Classical Venturi Determined Using Realizable K-Epsilon Two-Layer Turbulence Model.....	38
Figure 16. Gas Expansion Factors for 0.5 $\beta$ Classical Venturi.....	39
Figure 17. Gas Expansion Factors for 0.6 $\beta$ Classical Venturi.....	39
Figure 18. Incompressible Flow Discharge Coefficient Values for 0.4 $\beta$ Standard Concentric Orifice Plate .....	43
Figure 19. Incompressible Flow Discharge Coefficient Values for 0.5 $\beta$ Standard Concentric Orifice Plate .....	44

Figure 20. Incompressible Flow Discharge Coefficient Values for $0.6 \beta$ Standard Concentric Orifice Plate .....	45
Figure 21. Standard Concentric Orifice Plate Velocity Scene Showing Pressure Taps ...	45
Figure 22. Standard Concentric Orifice Plate Pressure Scene Showing Pressure Taps ...	46
Figure 23. Gas Expansion Factors for $0.4 \beta$ Standard Concentric Orifice Plate .....	49
Figure 24. Gas Expansion Factors for $0.5 \beta$ Standard Concentric Orifice Plate .....	50
Figure 25. Gas Expansion Factors for $0.6 \beta$ Standard Concentric Orifice Plate .....	51
Figure 26. Incompressible Flow Discharge Coefficient Values for $0.3789 \beta$ Wedge Meter .....	53
Figure 27. Incompressible Flow Discharge Coefficient Values for $0.5019 \beta$ Wedge Meter .....	54
Figure 28. Incompressible Flow Discharge Coefficient Values for $0.6107 \beta$ Wedge Meter .....	54
Figure 29. Gas Expansion Factors for $0.3789 \beta$ Wedge Meter.....	57
Figure 30. Gas Expansion Factors for $0.5019 \beta$ Wedge Meter.....	57
Figure 31. Gas Expansion Factors for $0.6107 \beta$ Wedge Meter.....	58
Figure 32. Gas Expansion Factors for A Variety of Differential Pressure Meters with $\beta$ Values of $0.3789$ .....	59
Figure 33. Classical Venturi Pressure Scene .....	60
Figure 34. Classical Venturi Velocity Scene. ....	60
Figure 35 Classical Venturi Density Scene .....	61
Figure 36. Standard Concentric Orifice Plate Pressure Scene .....	61
Figure 37. Standard Concentric Orifice Plate Velocity Scene.....	62
Figure 38. Standard Concentric Orifice Plate Density Scene .....	62
Figure 39. Wedge Meter Pressure Scene .....	63
Figure 40. Wedge Meter Velocity Scene .....	63

Figure 41. Wedge Meter Density Scene ..... 63

Figure 42. Gas Expansion Factor Mach Number Relationship ..... 65

## LIST OF SYMBOLS

$A_1$  = Cross sectional area of the upstream straight pipe

$A_2$  = Cross sectional area of the throat or bore of a differential pressure meter

$c$  = Celerity of the working fluid

$C_d$  = Discharge coefficient

$C_{d\_INC}$  = Incompressible flow discharge coefficient

$C_{d\_CMP}$  = Compressible flow discharge coefficient

$d$  = Diameter of the throat or bore of a differential pressure meter

$D$  = Diameter of the upstream straight pipe

$e$  = Thickness of the tip of a Standard Concentric orifice plate

$E$  = Thickness of the base of a Standard Concentric orifice plate

$g_c$  = Dimensional conversion constant,  $1\text{ kg} \cdot \text{m}/(\text{N} \cdot \text{s}^2)$

$g_l$  = local gravitational constant

$H$  = Wedge meter wedge segment height

$H_{EL}$  = Elevation above a datum

$J$  = Quantity of heat

$\dot{m}_{theo}$  = Theoretical mass flow rate

$\dot{m}_{actual}$  = True mass flow rate

$M$  = Mach number

$M_w$  = Molecular weight

$P_1$  = Pressure at the upstream pressure tap

$P_2$  = Pressure at the downstream pressure tap

$\Delta P$  = Differential pressure ( $P_1 - P_2$ )

$P_2/P_1$  = Differential pressure ratio

$Q$  = Net heat transferred into a system

$R_e$  = Reynolds number calculated with respect to D

$R_{e\_actual}$  = Reynolds number calculated with respect to D, using values extracted from simulation results

$R_o$  = Universal gas constant,  $8314.41 \text{ J}/(\text{g} \cdot \text{mol} \cdot \text{K})$

$R_w$  = Radius of curvature of wedge meter wedge apex

$T_f$  = Flowing absolute temperature

$u$  = Internal energy

$V$  = Velocity at a point

$\bar{V}$  = Average velocity

$W$  = Work

$Y_1$  = Adiabatic gas expansion factor calculated using density taken at the upstream pressure tap

$\alpha$  = angle of bevel of downstream face of Standard Concentric Orifice Plate

$\beta$  = Ratio of the throat or bore diameter to the upstream straight pipe diameter

$\beta_{actual}$  = Ratio of the throat or bore diameter to the upstream straight pipe diameter using dimensions measured from post mesh geometry

$\varepsilon$  = Gas expansion factor

$\varepsilon_B$  = Gas expansion factor calculated using the Buckingham equation

$\varepsilon_{RH}$  = Gas expansion factor calculated using the Reader-Harris equation.

$\theta_c$  = Angle of convergent section of Venturi meter, angle of wedge plane of wedge meter

$\theta_d$  = Angle of divergent section of Venturi meter

$\theta_1$  = Wedge meter upstream external angle

$\theta_2$  = Wedge meter downstream external angle

$\kappa$  = Isentropic exponent

$\mu$  = Absolute viscosity

$\rho_f$  = Density at flowing conditions

$\rho_1$  = Density at upstream pressure tap

$\phi$  = Random variable of interest

## CHAPTER I

### INTRODUCTION

The natural gas supply industry routinely uses differential pressure flow meters (DPFM) to measure the flow rate of natural gas (Kiš, Malcho, Janovcová, 2014). Accurate compressible flow measurement is essential to the proper operation and fiscal success of this industry. For example, assuming all the natural gas suppliers in the U.S. exclusively use DPFMs to measure flow rate a uniform -0.05% error in the measurement of natural gas delivery to industrial consumers would result in a profit loss of approximately 20 million dollars for natural gas suppliers (EIA, 2019). Therefore, minimizing compressible flow measurement error is very lucrative for natural gas suppliers.

DPFMs are calibrated to measure the flow rate of incompressible fluids. The gas expansion factor ( $\varepsilon$ ) is used to correct for the errors compressible fluids produce in these DPFM's flow rate measurements. However, equations that predict  $\varepsilon$  are not available for all DPFM designs.

Depending on DPFM geometry, either theoretical or empirical equations are used to predict  $\varepsilon$  for a given pressure differential. The laboratory experiments required to produce empirical  $\varepsilon$  equations are expensive to conduct and restricted in their application to specific DPFM geometries. Consequentially,  $\varepsilon$  equations currently exist for a small set of DPFM geometries. These DPFM geometries are restricted to Venturis, orifice plates, and cone meters (Miller, 1996; Stewart et al., 2001).

Therefore, the objective of this study is to investigate if computational fluid dynamics (CFD) can be used to predict  $\varepsilon$  values sufficiently accurate for use in the regression of accurate empirical  $\varepsilon$  equations for a variety of DPFM geometries. The existence of accurate empirical  $\varepsilon$  equations for DPFMs geometries currently without them would facilitate using these DPFMs for compressible flow metering, and, potentially, result in massive profits for the corresponding DPFMs' manufacture.

## CHAPTER II

### THEORETICAL BACKGROUND

DPFMs are fundamentally a constriction in the flow area of a closed conduit. The constriction in flow area produces flow acceleration which results in a local drop in line pressure. Flow rate can be calculated from these flow meters if the fluid density, the cross-sectional area available for flow upstream of the constriction, the cross-sectional area of the constriction, and the pressure differential produced by the flow meter are known (Miller, 1996). Mass flow rate ( $\dot{m}$ ) is calculated using Equation 1.

$$\dot{m} = \epsilon C_d \frac{\pi}{4} d^2 \sqrt{\frac{2g_c \Delta P \rho_1}{1 - \beta^4}} \quad (1)$$

Where  $C_d$  is the discharge coefficient,  $d$  is the diameter of the downstream plane,  $g_c$  is a dimensional conversion constant =1 ( $kg \cdot m$ )/( $N \cdot s^2$ ),  $\Delta P$  is the pressure differential between the upstream and downstream planes,  $\rho_1$  is the density measured at the upstream plane, and  $\beta$  is the ratio between the downstream and upstream planes' diameters.

Equation 1 can be used to calculate incompressible or compressible  $\dot{m}$ . The theoretical  $\dot{m}$  equation can be derived by applying Bernoulli's energy equation and mass flow continuity between an upstream ( $A_1$ ) and a downstream ( $A_2$ ) plane within a control volume as shown in Figure 1 (Equations 2-3) (Miller, 1996).

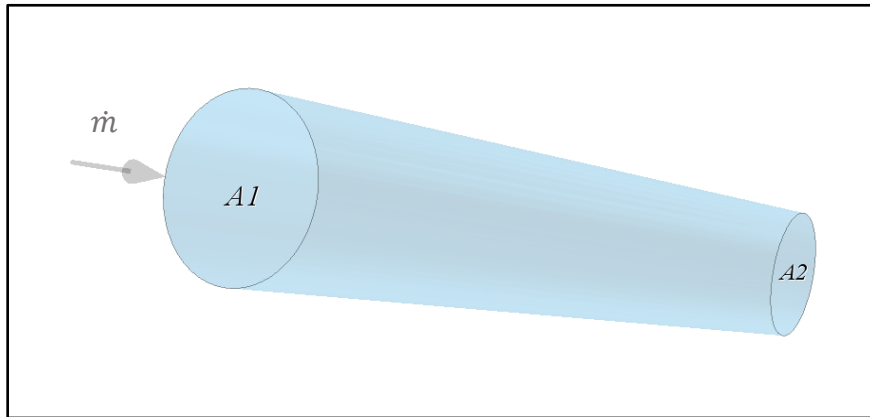


Figure 1. Control Volume.

$$\frac{P}{\rho} + \frac{\bar{V}}{2g_c} + \frac{g_l}{g_c} H_{EL} = \text{constant} \quad (2)$$

Where  $P$  is pressure,  $\bar{V}$  is the mean velocity,  $g_l$  is the local gravitational constant,  $H_{EL}$  is the elevation above the energy datum.

$$\dot{m} = \rho_1 A_1 \bar{V}_1 = \rho_2 A_2 \bar{V}_2 \quad (3)$$

Assuming constant density, uniform, steady, inviscid flow, and no elevation change between planes, and then substituting Equation 3 into Equation 2 yields Equation 4. In Equation 4, if  $A_1$  and  $A_2$  are circular, the ratio of their areas raised to the second power reduces to  $\beta$  raised to the fourth power. The  $\bar{V}$  at the downstream plane in Equation 4 is rewritten in terms of  $\dot{m}$  using Equation 3. Equation 4 is then solved for  $\dot{m}$ , yielding the theoretical mass flow rate ( $\dot{m}_{theo}$ ) equation for an incompressible fluid (Equation 5).

$$\frac{P_1 - P_2}{\rho} = \frac{\left[1 - \left(\frac{A_2}{A_1}\right)^2\right] \bar{V}_2^2}{2g_c} \quad (4)$$

$$\dot{m}_{theo} = \frac{\pi}{4} d^2 \sqrt{\frac{2g_c \Delta P \rho}{1 - \beta^4}} \quad (5)$$

The  $C_d$  is introduced to Equation 5 to account for  $A_2$  not being measured at the vena contracta,  $A_2$  and downstream pressure ( $P_2$ ) being measured at different planes, and for energy loss due to turbulence (Miller, 1996). The result is an equation which can be used to calculate the actual mass flow rate ( $\dot{m}_{actual}$ ) of an incompressible fluid through a DPFM (Equation 6).  $C_d$  for a given  $\dot{m}$  is the ratio of  $\dot{m}_{actual}$  to  $\dot{m}_{theo}$  (Equation 7).

$$\dot{m}_{actual} = C_d \frac{\pi}{4} d^2 \sqrt{\frac{2g_c \Delta P \rho}{1 - \beta^4}} \quad (6)$$

$$C_d = \frac{\dot{m}_{actual}}{\dot{m}_{theo}} < 1 \quad (7)$$

Regarding flow of a compressible fluid in a pressurized conduit, the contraction in flow area causes an increase in fluid velocity which results in a drop in pressure. Upon entering the zone of lower pressure, the fluid expands. Therefore,  $\epsilon$  is incorporated into Equation 6 to correct for the expansion of the fluid (Miller, 1996). The adiabatic gas expansion factor ( $Y$ ) can be derived from the thermodynamic steady flow energy equation (Equation 7). Through intensive algebraic manipulation, integration, and by assuming adiabatic expansion, isentropic flow, and no elevation difference between the upstream and downstream planes, Equation 8 reduces to Equation 9 where  $Y_I$  is defined in Equation 10 (Miller 1996).

$$Q - W = J(u_2 - u_1) + \frac{P_2}{\rho_2} - \frac{P_1}{\rho_1} + \frac{\overline{V_2^2} - \overline{V_1^2}}{2g_c} + \frac{g_l}{g_c} (H_{EL_2} - H_{EL_1}) \quad (8)$$

Where  $Q$  is the net heat transferred into a system,  $W$  is work,  $J$  a quantity of heat, and  $u_1$  and  $u_2$  are the internal energy at the upstream and downstream planes, respectively.

$$\dot{m}_{theo} = Y_1 \frac{\pi}{4} d^2 \sqrt{\frac{2g_c \Delta P \rho_1}{1 - \beta^4}} \quad (9)$$

Where  $Y_1$  is the theoretical adiabatic  $\varepsilon$  calculated from density measured at the upstream plane.

$$Y_1 = \left\{ \frac{\left[ 1 - \beta^4 \right] \left[ \frac{\kappa}{\kappa - 1} \right] \left( \frac{P_2}{P_1} \right)^{\frac{2}{\kappa}} \left[ 1 - \left( \frac{P_2}{P_1} \right)^{\frac{\kappa - 1}{\kappa}} \right]}{\left[ 1 - \beta^4 \left( \frac{P_2}{P_1} \right)^{\frac{2}{\kappa}} \right] \left( 1 - \frac{P_2}{P_1} \right)} \right\}^{\frac{1}{2}} \quad (10)$$

Where  $\kappa$  is the isentropic exponent of the working fluid.

In practice, compressible flows approach adiabatic expansion only in contoured DPFMs, such as the Classical Venturi, where expansion in the lower pressure zone is primarily axial (Miller, 1996). For DPFMs where flow expansion is both axial and radial,  $\varepsilon$  must be calculated using empirical methods. In general,  $\varepsilon$  is a function of the hydraulic shape of the flow meter,  $\beta$ , and  $\kappa$ .  $\varepsilon$  is also a function of the  $\Delta P$  produced by the DPFM at a given Reynolds Number ( $Re$ ) (Halmi, 1972).  $\varepsilon$  is defined as the ratio of the compressible discharge coefficient ( $C_{d\_CMP}$ ) to the incompressible discharge coefficient ( $C_{d\_INC}$ )

(Equation 11). Incorporation of  $\varepsilon$  into Equation 6 yields Equation 1.  $\varepsilon$  is equal to one for incompressible flows (Miller, 1996).

$$\varepsilon = \frac{\varepsilon C_d}{C_d} = \frac{C_{d\_CMP}}{C_{d\_INC}} \leq 1 \quad (11)$$

## CHAPTER III

### LITERATURE REVIEW

There has been extensive work regarding the determination of empirical  $\varepsilon$  values for DPFMs, specifically standard concentric (SC) orifice plates. Buckingham (1932) produced the first empirical  $\varepsilon$  equation for SC orifice plates (Equation 13). Buckingham's equation is based on data from experiments conducted in 1929 at the Los Angeles Gas and Electric Company. These experiments used natural gas as the working fluid. Equation 13 was adopted by both the American Gas Association (AGA Report No. 3) and the International Organization for Standardization (ISO 1567) and used for over 60 years (Morrow, 2004).

$$\varepsilon_B = 1 - (0.41 + 0.35\beta^4)\left(1 - \frac{P_2}{P_1}\right)\frac{1}{\kappa} \quad (13)$$

Where  $\varepsilon_B$  is the  $\varepsilon$  value calculated using Buckingham's equation.

Murdock and Foltz (1956) conducted orifice gas expansion experiments, using steam as the working fluid, and found the  $\varepsilon$  values predicted by Equation 13 to be an acceptable match with their results. However, during a review of SC orifice plate  $\varepsilon$  data from the European Economic Community (EEC) orifice coefficient program, Kinghorn (1986) noticed  $\varepsilon$  values calculated using Equation 13 were low by as much as 0.5%. In response Kinghorn recommend the development of a new SC orifice plate  $\varepsilon$  equation from existing and new experimental data. At the Colorado Engineering Experiment Station (CEESI),

Seidl (1995) conducted SC orifice plate  $\varepsilon$  experiments using air as the working fluid.

Seidl also noticed that Equation 13 underpredicted  $\varepsilon$  values.

Reader-Harris (1998) derived a new empirical SC orifice plate  $\varepsilon$  equation from the EEC orifice coefficient program and CEESI data (Equation 14). In 2003, ISO adopted Equation 14 in *ISO 5167-2:2003*. Equation 14 is currently ISO's and the ASME's recommend SC orifice plate  $\varepsilon$  equation (ASME, 2007). However, the validity of Equation 14 was initially questioned because of the relative sparseness of data used to produce it. Therefore, Morrow (2004) conducted additional SC orifice plate  $\varepsilon$  experiments at the South West Meter Institute's Meter Research Station. Data from Morrow's experiments fell within the specified 95% confidence intervals of both Equation 13 and 14. Morrow also noticed that the  $\varepsilon$  values predicted by Equation 14 fall almost exactly on the upper uncertainty limit of Eq 13.

$$\varepsilon_{RH} = 1 - (0.351 + 0.256\beta^4 + 0.93\beta^8) \left[ 1 - \left( \frac{P_2}{P_1} \right)^{\frac{1}{k}} \right] \quad (14)$$

Where  $\varepsilon_{RH}$  is the  $\varepsilon$  value calculated using the Reader-Harris equation.

There are also several CFD related publications that are related to this studies research objectives. Specifically, these publications are concerned with CFD's ability to predict DPFMs'  $C_d$  and  $\varepsilon$  values. Hollingshead et al. conducted a CFD study, using the commercial code FLUENT, on the  $C_{d\_INC}$  performance of Venturi, SC orifice plate, cone meter, and wedge flow meters (2011). The  $Re$  values of the DPFM simulations ranged from 1 to  $10^7$ . Upon comparison with laboratory data, the simulation results adequately

characterized each meter's  $C_{d\_INC}$  performance trend as a function of  $Re$ . However, the predicted  $C_{d\_INC}$  values were not an exact match with laboratory  $C_{d\_INC}$  data, and routinely exhibited magnitudes of error unacceptable in industrial and municipal flow metering applications.

Sharp (2016) conducted a CFD study, using the commercial code STAR CCM+, to address several Venturi meter design problems. The study's CFD simulations were calibrated and validated using laboratory data from experiments conducted at the Utah State Water Research Lab. Sharp also found CFD can be appropriately used to determine performance trends or relative differences associated with changes in meter design. However, Sharp also acknowledges "...CFD is not a replacement for laboratory calibration" (2016).

Prasanna et al. (2016), in two separate studies, showed the commercial CFD code ANSYS FLUENT-14 can be used to adequately predict  $\varepsilon$  values for Classical Venturi and SC orifice plate meters. The DPFMs were modeled using 2D axisymmetric simulations. Simulation  $Re$  values were kept constant and  $\beta$  values and line pressure were varied to produce a variety of  $\varepsilon$  values. Comparison of Prasanna et al.'s six CFD Venturi  $\varepsilon$  values to the  $\varepsilon$  predicted by Equation 10 shows a minimum percent difference of 0.12%, an average percent difference of 0.58%, and a maximum percent difference of 1.2%. Comparison of Prasanna et al.'s five CFD SC orifice plate  $\varepsilon$  values to  $\varepsilon$  values predicted by Equation 14 shows a minimum percent difference of 0.09%, an average percent difference of 1.15%, and a maximum percent difference of 2.4%. Percent difference for parameter of interest ( $\phi$ ) is calculated throughout this paper as shown in Equation 15.

$$\frac{(\phi_{\text{calculated}} - \phi_{\text{theoretical}})}{\phi_{\text{theoretical}}} \times 100\% \quad (15)$$

## CHAPTER IV

### RESEARCH OBJECTIVES

There are no existing publications regarding the use of CFD to predict  $\varepsilon$  values for wedge meters. In addition, an experimentally derived  $\varepsilon$  equation for wedge meters does not exist (ISO, 2019). ISO-6:2019 recommends using (Equation 10) to estimate wedge meter  $\varepsilon$  values. Therefore, this study has been conducted with the following research objectives:

1. Model incompressible and compressible flows through Classical Venturi and SC orifice plate geometries, with  $\beta$  values of 0.4, 0.5, and 0.6, using the commercial CFD code STAR CCM+.
2. Corroborate incompressible and compressible flow simulation methods for Classical Venturi and SC orifice plate geometries based on the comparison of CFD  $C_{d\_INC}$  and  $\varepsilon$  values to the  $C_{d\_INC}$  and  $\varepsilon$  values predicted by ASME or ISO endorsed equations.
3. Using the same modeling approach employed to model incompressible and compressible flows through Classical Venturi and SC orifice plates, model incompressible and compressible flows through wedge meter geometries with 1 mm (0.03937 in.) filleted wedge apexes and  $\beta$  values of approximately 0.3789, 0.5019, and 0.6107.
4. Corroborate incompressible flow simulations for wedge meters based on the comparison of CFD  $C_{d\_INC}$  values to the  $C_{d\_INC}$  values predicted by an ISO endorsed equation.
5. Use wedge meter CFD simulation results to calculate wedge meter  $\varepsilon$  values.

## CHAPTER V

### SIMULATION SETUP

The following sections describes the setup of this study's simulations. First, the established method to determine DPFMs' compressible flow discharge coefficients is reviewed. Then a list of the physics models used to simulate incompressible and compressible flows are presented. Next the methods used to determine the ranges and values of simulation flow properties, material properties, and boundary conditions are described. Then the dimensions and meshing methods for each DPFM geometry and  $\beta$  values are presented. In addition, the parameters extracted from CFD simulations and the methods used to calculate  $C_d$ ,  $\varepsilon$ , and  $R_{e\_actual}$  are described. Finally, the criteria used to establish mesh independence and adequate convergence for all CFD simulations are explained.

#### **Established Method to Determine Compressible Flow Discharge Coefficients in a Laboratory Setting**

The ideal gas law (Equation 16) is an appropriate model of real gas behavior for gases at high temperatures and low pressures relative to the gas' critical temperature and pressure (LeTran, 2020). During the 1929, Los Angeles Gas and Electric Company  $\varepsilon$  experiments Buckingham restricted experimental testing conditions such that the flow of natural gas, the working fluid, could be reasonably modeled as an isentropic flow of an ideal gas (1932). Absolute line pressure was kept below 263.52 kPa (38.22 psia), and flow  $R_e$  was held above 200,000 so that flow at the vena contracta was nearly isentropic (Buckingham, 1932).

$$\rho_f = \frac{M_w P_f}{R_o T_f} \quad (16)$$

Where  $M_w$  is molecular weight,  $R_o$  is the universal gas constant,  $T_f$  is the absolute temperature at flowing conditions,  $\rho_f$  is the density at flowing conditions, and  $P_f$  is the pressure at flowing conditions.

Buckingham also stated that an SC orifice plate's  $C_{d\_INC}$  was sensibly independent of the rate of flow at  $Re$  higher than 200,000. Consequentially, Buckingham treated the variation in  $C_{d\_CMP}$  with  $Re > 200,000$  as a function of compressibility alone (Buckingham, 1932). However, for  $Re > 200,000$ , the variation of SC orifice plates'  $C_{d\_INC}$  is significant in the calculation of accurate  $\varepsilon$  values (Morrow, 2004).

The current established method for obtaining a range of  $C_{d\_CMP}$  values to be used in the calculation of  $\varepsilon$  values is to hold  $Re$  constant and adjust line pressure and  $\dot{m}$  to obtain different  $C_{d\_CMP}$  values. Flow conditions the ideal gas law can be reasonably applied to are maintained throughout this process. This ensures the change in  $C_{d\_CMP}$ , and the resulting value of  $\varepsilon$ , are solely dependent on the compressibility of the working fluid (Morrow, 2004).

### **Physics Models**

The physics models used for incompressible and compressible flow simulations are shown in Table 1. There is an exception to the models shown in Table 1 for Classical Venturi simulations. These meters were modeled primarily using a combination of

axisymmetric and three-dimensional space with both methods agreeing well with each other. It is also important to note air was modeled as a perfect gas even though the equation of state selected was the ideal gas law. An ideal gas' specific heat is a function of temperature. A perfect gas' specific heat is held constant (Miller, 1996). For detailed explanation of the physics models in Table 1 refer to Simcenter STAR-CCM+ documentation (Siemens, 2020).

Table 1. STAR-CCM+ Physics Models.

Model Category	Incompressible Flow	Compressible Flow
Space	Three Dimensional	Three Dimensional
Time	Steady State	Steady State
Material	Liquid (water)	Gas (dry air)
Equation of State	Constant Density	Ideal Gas (perfect gas)
Flow Solver	Segregated	Segregated
Pressure Solver	SIMPLE	SIMPLE
Energy	None	Segregated Fluid Temperature
Viscous Regime	Turbulent	Turbulent
RANS Turbulence	Realizable K-Epsilon Two-Layer	Realizable K-Epsilon Two- Layer
Wall Distance	Wall Distance	Wall Distance
Gradient Metrics	Gradients	Gradients
Wall Treatment	Two-Layer All y+ Wall Treatment	Two-Layer All y+ Wall Treatment

### Determination of Simulation Parameters and Flow Conditions

The selection of simulation parameters and flow conditions differed for incompressible and compressible flow models with one exception. Flow in incompressible and compressible simulations was restricted to subsonic velocities (i.e Mach number ( $M$ )  $\leq 0.75$ ).  $M$  was calculated locally at each cell in the simulations computational mesh. using Equation 17. The computational mesh is the discretized geometry created

from the mathematically defined computer aided drafting (CAD) DPFM surface. During discretization the CAD surface and the volume it contains are broken into a multitude of cells which collectively form the computational mesh.

$$M = \frac{V}{c} \quad (17)$$

Where  $V$  is a point velocity equivalent to the average velocity across a cell and  $c$  is the celerity of the working fluid.

**Incompressible Flow.** The material properties of water applicable to this study's simulations are  $\rho$  and  $\mu$ .  $\rho$  and  $\mu$  were varied to maintain lower flow velocities at high  $R_e$  values. Lower flow velocities tended to result in better simulation convergence. To simulate water with a temperature of 299.82 K (80 °F),  $\rho$  was set as 996.60 kg/m<sup>3</sup> (62.22 lbm/ft<sup>3</sup>) and  $\mu$  as  $8.58 \times 10^{-4}$  Pa-s ( $8.46 \times 10^{-9}$  atm-s). To simulate water with a temperature of 366.48 K (200 °F), water  $\rho$  was set as 969.78 kg/m<sup>3</sup> (60.54 lbm/ft<sup>3</sup>) and  $\mu$  as  $3.03 \times 10^{-4}$  Pa-s (2.99107e-9 atm-s).

**Compressible Flow.** To ensure isentropic flow at the vena contracta, simulation inlet boundary  $R_e$  values ranged from 230,000 to 1,150,000. To ensure the working fluid, dry air, could be reasonably modeled as a perfect gas, pressure was set low relative to dry air's critical pressure of 3.77 MPa (546.65 psi) and temperature was set high relative to dry air's critical temperature of 132.7 K (-220.8 °F) (Miller, 1996). Absolute static pressure ranged from to approximately 172.37 kPa (25 psia) to 262 kPa (38 psia) and static temperature was set as 299.82 K (80 °F) for all simulations.

The material properties applicable to this study's air simulations are  $M_w$ , turbulent Prandtl number, specific heat, thermal conductivity,  $\mu$ , and  $\kappa$ . All of these properties, except  $M_w$ , change within the dynamic conditions that occur in flow through DPFMs. Therefore, material properties of air, except  $M_w$ , must either be calculated for each iteration of the simulation or approximated as constant. Dry air's material properties were set as constant for each iteration of the simulation. For all simulations  $M_w$  was set as 28.9664 g/gmol and Turbulent Prandtl number was set to a value of 0.9. Depending on the static pressure boundary conditions specific heat was linearly interpolated between 1.0061 kJ/(kg-K) at 101.35 kPa (14.7 psia) and 1.0162 kJ/(kg-K) at 709.47 kPa (102.9 psia), and thermal conductivity was linearly interpolated between the two values of 26.37 mW/(m-K) at 99.97 kPa (14.5 psia) and 27.01 mW/(m-K) at 2.0 MPa (290 psia).  $\mu$  for a given static pressure was determined by linearly interpolating between two equations produced from curve fits of  $\mu$  data taken at constant pressure and varying temperature (Figure 2).  $\kappa$  was assumed to have a constant value of 1.4.

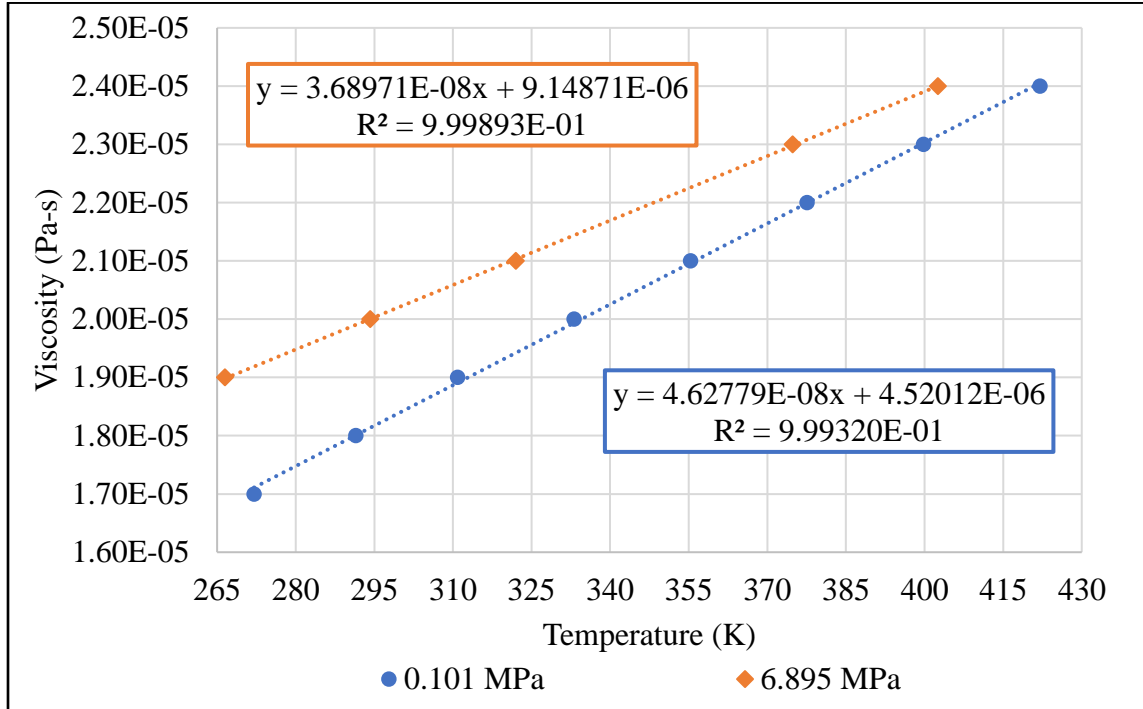


Figure 2. Absolute Viscosity of Air at Different Static Pressures (Miller 1996).

### Calculation or Selection of Simulation Boundary Values

Appropriate selection of a CFD simulation's boundary conditions is crucial for obtaining results that are representative of the fluid phenomena of interest. Every simulation conducted in this study had the same three boundary types: velocity inlet, pressure outlet, and walls.

**Velocity Inlet Boundary.** The velocity inlet boundary's turbulent dissipation rate, turbulent kinetic energy, velocity vectors, and, for compressible flows, static temperature values were specified using a fully developed flow profile (FDFP) table for each mesh cell constituting the velocity inlet boundary. Unique FDFP tables were created from

FDFP simulations for each DPFM simulation's targeted  $R_e$  and  $\dot{m}$ .  $\dot{m}$  was calculated using Equation 18.

$$\dot{m} = \frac{\pi}{4} \mu D R_e \quad (18)$$

FDFP simulation geometry consisted of a 30.48 cm (12 in.) diameter cylinder that was 91.44 cm (36 in.) to 121.92 cm (48 in.) long. One end of the cylinder was set as a mass flow inlet boundary and the other end as a pressure outlet boundary. The inlet's  $\dot{m}$  was set equal to the respective target value calculated using Equation 18. A periodic, fully developed, mass flow interface was created between the mass flow inlet and the pressure outlet. This periodic interface essentially creates an infinite pipe in which a FDFP can develop. Upon solution convergence, a FDFP table was created by extracting the desired scalar values and their positions in model space from each mesh cell constituting the mass flow inlet interface.

**Pressure Outlet Boundaries.** For all incompressible flow simulations, pressure outlet boundary pressure was arbitrarily set at 1.38 MPa (200 psi). For all compressible flow simulations, pressure outlet boundary pressure was set to the pressure used to calculate air's  $\rho$  in Equation 16.

**Wall Boundaries.** Wall boundaries were modeled as smooth, nonslip surfaces.

## **DPFM Dimensions and Mesh Generation**

All DPFM geometries were drafted in STAR CCM+'s 3D CAD environment. Pressure tap geometry was not included in any of the DPFMs geometries. However, the locations where static pressure values were extracted was consistent with ASME or ISO meter standards and are presented in the following sections. A 30.48 cm (12 in.) diameter cylinder was used for all DPFMs' upstream and downstream straight pipe geometry. All meshes were generated from CAD geometry using STAR CCM+ meshing operations.

Slight geometric distortion is an unavoidable consequence of creating a finite volume or area computational mesh from a mathematically defined CAD surface. This process is known as discretization. Therefore, the dimensions of the DPFMs presented in the following sections closely approximate post mesh geometry and are the dimensions of the mesh's source CAD geometry. Due to the use of a FDFP table at each simulation's velocity inlet, the upstream straight pipe of each DPFM geometry can be considered as sufficient in length for a FDFP to develop. For more information on meshing refer to Simcenter STAR-CCM+ documentation (Siemens, 2020).

**Classical Venturi Meter Dimensions.** Classical Venturi geometries with  $\beta$  values equal to 0.4, 0.5, and 0.6 were drafted in accordance with *ASME MFC-3Ma-2007* specifications (2007). The transitions of the entrance cylinder to the convergent and the convergent to the throat were modeled as sharp. A side view of a Classical Venturi is shown in Figure 3. Table 2 contains the dimensions for each Classical Venturi geometry per  $\beta$  value. For all Classical Venturi  $\beta$  values, upstream straight pipe length was 304.8 cm (120 in.) and

downstream straight pipe length was 121.92 cm (48 in.). Pressure was extracted at the standard pressure tap locations of  $1D$  upstream from the start of the convergent section and at the midpoint of the throat ( $d/2$ ).

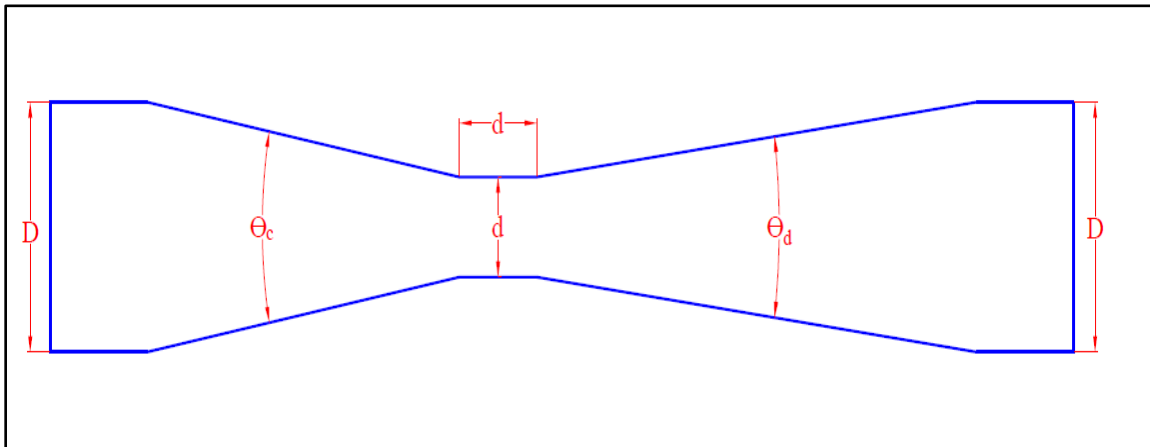


Figure 3. Classical Venturi with Sharp Transitions.

Table 2. Classical Venturi Dimensions (units in cm or degrees).

$\beta$	0.4	0.5	0.6
$D$	30.48	30.48	30.48
$d$	12.19	15.24	18.29
$\theta_c$	21°	21°	21°
$\theta_d$	15°	15°	15°

**Classical Venturi Meshing.** Flows through Classical Venturis were primarily modeled as axisymmetric. Therefore, Classical Venturi meshes were two-dimensional, longitudinal profiles of half of the Classical Venturi's CAD geometry as shown in Figure 4. The mesh consisted of two cell types as shown in Figure 5. The core mesh consisted of polyhedral shaped cells. Prism layer cells were used near wall boundaries. Prism layer cells are right rectangular prism shaped volume mesh cells. Cell base size was typically 0.635 cm (0.25 in.). Prism layer 1<sup>st</sup> cell thickness was adjusted for the High Ywall+

model such that the  $Y_{wall+}$  values were between 30 and 160. Typical mesh cell count was approximately 20,000 cells.



Figure 4. Classical Venturi 0.4  $\beta$  Half Profile

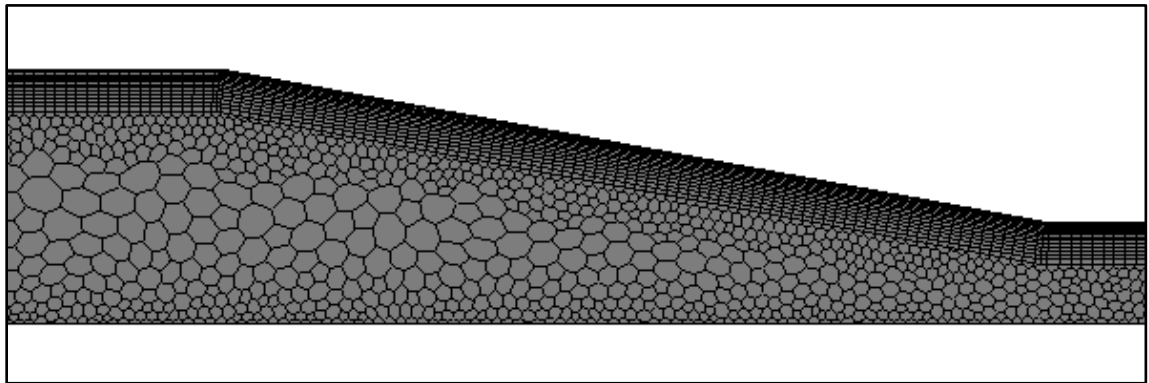


Figure 5. Classical Venturi Mesh.

**Standard Concentric Orifice Plate Meter Dimensions.** SC orifice plate geometries with  $\beta$  values equal to 0.4, 0.5, and 0.6 were drafted in accordance with *ASME MFC-3Ma-2007* specifications (2007). Figure 6 shows a SC orifice plate geometry profile annotated with *ASME MFC-3Ma-2007* symbology. Table 3 contains the dimensions for each standard concentric orifice plate geometry per  $\beta$  value. Pressure was extracted at ISO standard pressure tap locations of  $D$  and  $D/2$ , flange taps, and corner taps (2003).

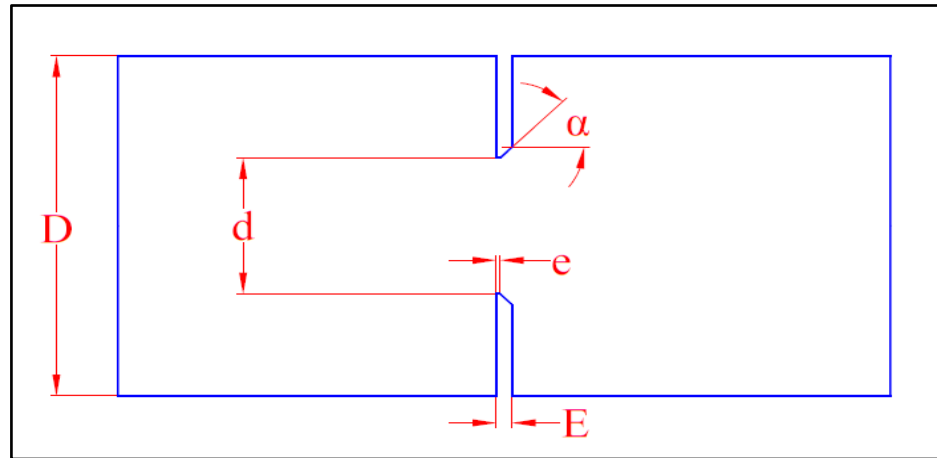


Figure 6. Standard Concentric Orifice Plate Profile.

Table 3. Standard Concentric Orifice Plate Dimensions (units in cm or degrees).

$\beta$	0.4	0.5	0.6
$D$	30.48	30.48	30.48
$d$	12.19	15.24	18.29
$E$	1.27	1.27	1.27
$e$	0.125	0.125	0.125
$\alpha$	45°	45°	45°

**Standard Concentric Orifice Plate Meter Meshing.** Three-dimensional meshes were generated from each SC orifice plate CAD geometry. The meshes consisted of two cell types. The core mesh consisted of trimmer cells. Trimmer cells are cube shaped volume mesh cells. Prism layer cells were used near wall boundaries. The cell base size was typically 1.27 cm (0.5 in). Volumetric controls were used to refine the mesh locally at the orifice edge tip as shown in Figure 7. A volumetric control is a CAD surface which is strategically placed to encompass a region of the computational mesh which requires additional refinement. The mesh generation algorithm refines mesh cells located within the volumetric control according to user specifications. Prism layer 1<sup>st</sup> cell thickness was adjusted for the High Ywall+ model such that the Ywall+ values were between 30 and

160 for the vast majority of the mesh cells constituting wall boundaries. A mesh consisting of elongated trimmer and prism cells was generated at the inlet and outlet of the simulation domain to extrude the mesh generated from CAD geometry to obtain a minimum  $2D$  of straight pipe upstream of the inlet and  $6D$  downstream of the outlet. Higher  $Re$  number simulations had longer outlet mesh extrusions to capture the corresponding increased length of the high velocity jet and recirculation zone downstream of the orifice. Typical mesh cell count was approximately 2 to 3 million cells.

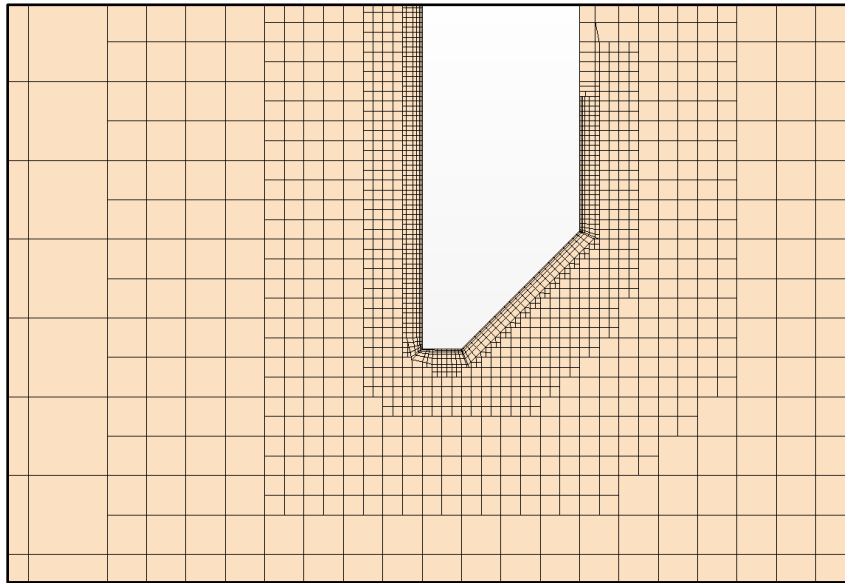


Figure 7. Cross Sectional View of a Standard Concentric Orifice Plate's Tip Mesh.

**Wedge Meter Dimensions.** Wedge geometries with  $\beta$  values approximately equal to 0.3789, 0.5019, and 0.6107 were drafted in accordance with *ISO 5167-6:2019* specifications (2019). Figure 8 shows a wedge meter profile annotated with *ISO 5167-6:2019* symbology. For all wedge meter geometries, the wedge apex was filleted with a radius of curvature ( $R_w$ ) equal to 1 mm (0.03937 in.). Table 4 contains the dimensions of

each wedge meter geometry per  $\beta$  value prior to meshing. Pressure was extracted at ISO standard pressure tap locations of 1D upstream from the start of wedge and 1D downstream from the end of the wedge (2019).

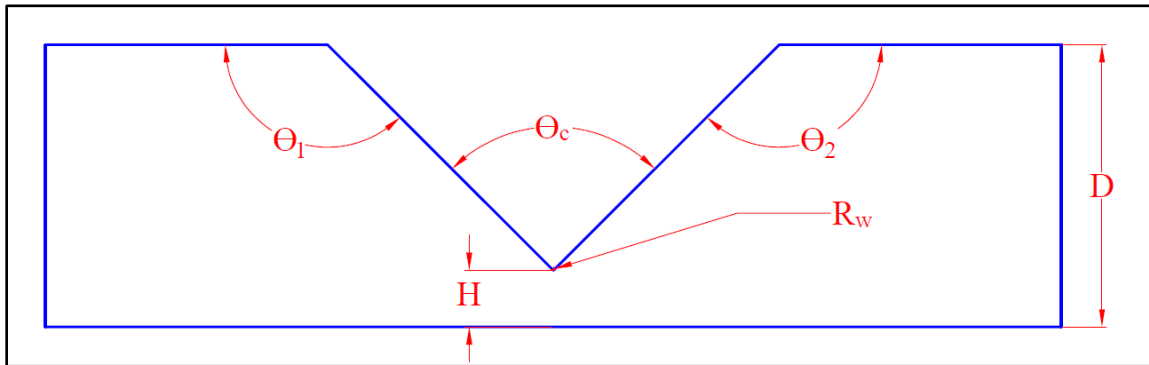


Figure 8. Wedge Meter Side View.

Table 4. Wedge Meter Dimensions (units in cm or degrees).

$\beta$	0.3789	0.5019	0.6107
D	30.48	30.48	30.48
H	6.1317	9.1342	12.1776
$R_w$	0.01	0.01	0.01
$\theta_c$	90°	90°	90°
$\theta_1 = \theta_2$	135°	135°	135°

**Wedge Meter Meshing.** Three-dimensional meshes were generated from each wedge meter 3D CAD geometry. The meshes consisted of two cell types. The core mesh consisted of polyhedral cells and prism layers were used near wall boundaries. Cell base size was typically 1.7961 cm (0.70711 in.). Volumetric controls were used to refine the core and prism layer mesh cells near the wedge apex, as shown in Figure 9. Prism layer 1<sup>st</sup> cell thickness was adjusted for the Low Ywall+ model such that the Ywall+ values were between 0.05 and 5, with a target value of 1, for the vast majority of the mesh

surface. An extruder mesh consisting of elongated polyhedral and prism cells was generated at the outlet of the simulation domain to obtain a minimum of  $6D$  downstream of the outlet, as partially shown in Figure 10. Typical mesh cell count was approximately 1.5 million cells.

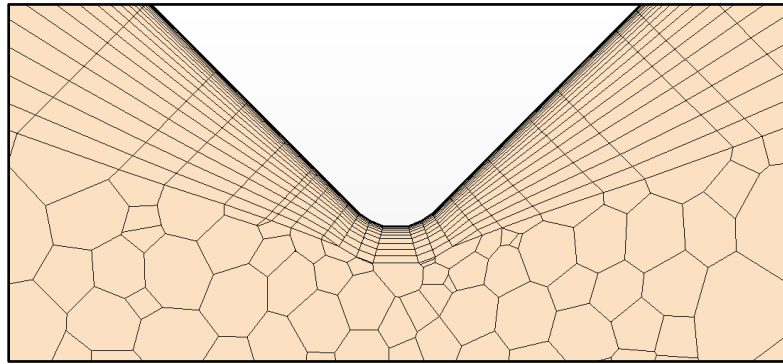


Figure 9. Cross Section of Wedge Meter Wedge Apex Mesh

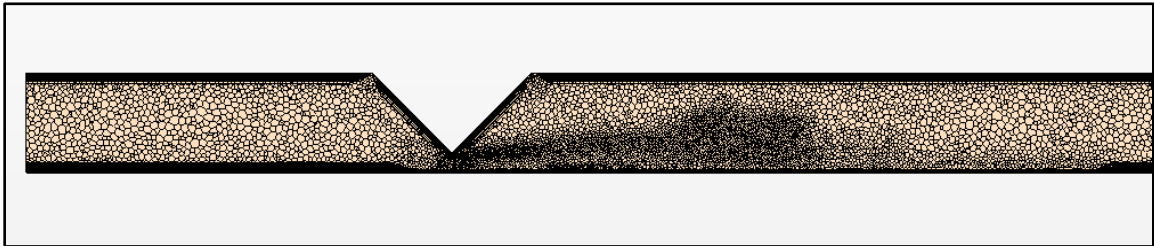


Figure 10. Cross section of  $0.3789 \beta$  Wedge Meter Mesh

### Simulation Parameters of Interest and Calculation of $\beta_{\text{actual}}$ , $\text{Re}_{\text{actual}}$ , $C_d$ , and $\varepsilon$

Flow property parameters, such as velocity or pressure, are spatially defined and stored at each mesh cell's centroid and faces (Siemens, 2020). Therefore, to extract the magnitude of  $\phi$  at a specific location, a derived part point or surface was defined such that it intersected the DPFM mesh at the point or plane of interest. A derived point or part is a CAD surface which intersects the computational mesh at a user specified location. The

derived part has no impact on the structure of the computational mesh and can be used to extract the value of  $\phi$  at a specific point or extract a range of  $\phi$  values across a plane.

The flow property parameters extracted from all DPFM simulations were  $\dot{m}$ ,  $P$ , and  $\rho$ .

$\dot{m}$  was extracted at velocity inlet boundaries.  $P$  was extracted using derived points placed at the respective DPFM's standard pressure tap locations.  $\rho$  was extracted from the derived point placed at the standard upstream pressure tap location. In addition, derived parts or simulation boundaries were used to extract the cross-sectional area of a given DPFM's computational mesh geometry. The cross-sectional area of the upstream pipe ( $A_1$ ) was extracted at the velocity inlet boundary. The cross-sectional area ( $A_2$ ) was extracted from a derived plane located at the DPFM geometry's minimum cross-sectional area.

$\beta_{actual}$ ,  $Re_{actual}$ ,  $C_{d\_INC}$ ,  $C_{d\_CMP}$ , and  $\varepsilon$  were calculated in a spreadsheet using the extracted values.  $\beta_{actual}$  was calculated using Equation 19.  $Re_{actual}$  was calculated using Equation 18.  $C_{d\_INC}$  and  $C_{d\_CMP}$  were calculated using equation 7. The calculation of  $\varepsilon$  was not as straight forward.

$$\beta_{actual} = \left( \frac{A_2}{A_1} \right)^{\frac{1}{2}} \quad (19)$$

Empirical  $\varepsilon$  equations are a function of  $\Delta P/P_1$  or  $P_2/P_1$  as well as  $\beta$  values and  $\kappa$ . In practice, calculation of  $\varepsilon$  using empirical equations is conservatively restricted to a range of  $P_2/P_1 \geq 0.8$  or  $0.75$  (ASME, 2007; ISO 2003). Therefore,  $\varepsilon$  values over a similar  $P_2/P_1$  range were desired for this study. However, the desired range of  $P_2/P_1$  could not

be acquired by holding  $Re$  constant and only varying line pressure and  $\dot{m}$ , as specified by Morrow (2004). Simulation solutions tended to diverge when absolute pressure was less than approximately 172.37 kPa (25 psia). In addition, exact matches of the  $Re$  values of the incompressible and compressible flow simulations could not be obtained. Therefore, a method was designed to ensure that the change in  $C_{d\_CMP}$  when compared to  $C_{d\_INC}$ , was restricted as much as possible to compressibility alone.

**Gas Expansion Factor Calculation Method.** The steps of method are as follows:

1. The performance trend in  $C_{d\_INC}$  versus  $Re$  was sufficiently resolved such that  $C_{d\_INC}$  could be reasonably interpolated for any  $Re$  value within the range of  $2.3 \times 10^5 \leq Re \leq 1.5 \times 10^6$ .
2. Incompressible flow simulations' meshes were adjusted and refined until the performance trend of the CFD  $C_{d\_INC}$  and the  $C_{d\_INC}$  predicted by ASME and ISO endorsed equations were similar adequately close in value.
3. Trendlines were fit to  $C_{d\_INC}$  versus  $Re$  scatter plots.
4. Compressible flows'  $\dot{m}$  and pressure were systematically varied until  $C_{d\_CMP}$  values were obtained over a range of absolute pressure ratios.
5. Using an equation representative of the trendline generated in step 3,  $C_{d\_INC}$  values were interpolated at the exact  $Re_{actual}$  values  $C_{d\_CMP}$  were computed at.
6. An  $\varepsilon$  value was then calculated from the  $C_{d\_CMP}$  and  $C_{d\_INC}$  values using Equation 11.
7. For Classical Venturi and SC orifice plate simulations, compressible flow simulation meshes were adjusted and refined until the value of  $\varepsilon$  predicted by

CFD and the value of  $\varepsilon$  predicted by ASME and ISO endorsed equations were acceptably close.

### **Mesh Independence and Acceptable Convergence Criteria**

To ensure the mesh independence of a given simulation's solution, Grid Convergence Index (GCI) studies were performed for incompressible and compressible flow simulations for each DPFM geometry and  $\beta$  value according to the method described in "Procedure for estimation and reporting of uncertainty due to discretization in CFD applications" (ASME 2008). Acceptable  $GCI_{\text{fine}}$  was specified as less than 3%. The majority of  $GCI_{\text{fine}}$  values were less than 0.1%. All GCI study results are presented in the appendix.

Acceptable simulation solution convergence was achieved when the normalized residuals of turbulent kinetic energy, turbulent dissipation rate, continuity, momentum, and energy were reduced to at least the order of  $10^{-3}$ . This was defined as the minimum acceptable normalized residual convergence. Normalized residuals typically reduced at least to the order of  $10^{-5}$ .

Acceptable simulation solution convergence was also determined by monitoring the flow parameter values of  $\dot{m}$ ,  $P$ ,  $\rho$ , and maximum and average  $V$ . At each iteration, these values were extracted the same derived parts and boundaries used to calculate  $\beta_{\text{actual}}$ ,  $Re_{\text{actual}}$ ,  $C_d$ ,  $\varepsilon$ . When the values of  $\dot{m}$ ,  $P$ ,  $\rho$ , and maximum and average  $V$  remained constant for over 1000 iterations the solution was considered converged.

## CHAPTER VI

### RESULTS AND DISCUSSION

The following sections present and discuss simulation results for each DPFM geometry.

All  $P_2/P_1$  ratios in tabulated data and plots are calculated using absolute pressures.  $C_{d\_INC}$  or  $\varepsilon$  values predicted using ASME or ISO endorsed equations are referred to as theoretical values.

#### **Classical Venturi Meter**

In this section, Classical Venturi Meter simulation's  $C_{d\_INC}$  and  $\varepsilon$  values for  $\beta$  values of 0.4, 0.5, and 0.6 are presented. Computed  $C_{d\_INC}$  values are compared to the theoretical  $C_{d\_INC}$  value of 0.995. The  $C_{d\_INC}$  value of 0.995 is from the ASME  $C_{d\_INC}$  equation for a Venturi Tube with a machined convergent section (Equation 20). The relative uncertainty of Equation 20 is 1%, expressed at a 95% confidence interval (ASME 2007). The ASME Venturi Tube is analogous to a Classical Venturi (ASME 2007). CFD  $\varepsilon$  values are compared against theoretical  $\varepsilon$  values predicted using Equation 10.

$$C_{d\_INC} = 0.995 \quad (20)$$

$$10.16 \text{ cm} \leq D \leq 121.92 \text{ cm}$$

$$0.3 \leq \beta \leq 0.75$$

$$2 \times 10^5 \leq R_e \leq 6 \times 10^6$$

To determine  $\varepsilon$ 's sensitivity to the type of turbulence model used, several 0.4  $\beta$  Classical Venturi simulations are repeated using turbulence models other than the Realizable K-

Epsilon Two-Layer turbulence model. These turbulence models are Standard Spalart-Allmaras, SST(Menter) K-Omega, and Reynolds Stress Turbulence with Elliptic Blending. Refer to Simcenter STAR-CCM+ documentation for more information on these turbulence models (Siemens, 2020).

**Classical Venturi Incompressible Flow Simulations.** Classical Venturi  $C_{d\_INC}$  values for  $\beta$  values of 0.4, 0.5, and 0.6 simulations are presented in this section (Tables 5-10, Figures 11-13).

Table 5. Incompressible Flow Discharge Coefficient Values for 0.4  $\beta$  Classical Venturi Determined Using Realizable K-Epsilon Two-Layer Turbulence Model.

$Re$	$C_{d\_INC}$	$C_{d\_INC}$ (Eq. 19)	% Dif
229952	0.9860	0.995	-0.906%
415021	0.9860	0.995	-0.900%
599835	0.9861	0.995	-0.898%
649980	0.9862	0.995	-0.888%

Table 6 Incompressible Flow Discharge Coefficient Values for 0.4  $\beta$  Classical Venturi Determined Using Standard Spalart-Allmaras Turbulence Model.

$Re$	$C_{d\_INC}$	$C_{d\_INC}$ (Eq. 19)	% Dif
415021	0.9943	0.995	-0.067%
599835	0.9946	0.995	-0.040%
650200	0.9941	0.995	-0.090%

Table 7. Incompressible Flow Discharge Coefficient Values for 0.4  $\beta$  Classical Venturi Determined Using SST(Menter) K-Omega Turbulence Model.

$Re$	$C_{d\_INC}$	$C_{d\_INC}$ (Eq. 19)	% Dif
415022	0.9866	0.995	-0.846%
599835	0.9857	0.995	-0.932%
650200	0.9858	0.995	-0.930%

Table 8. Incompressible Flow Discharge Coefficient Values for 0.4  $\beta$  Classical Venturi Determined Using Reynolds Stress Turbulence with Elliptic Blending Turbulence Model.

$Re$	$C_{d\_INC}$	$C_{d\_INC}$ (Eq. 19)	% Dif
415021	0.9878	0.995	-0.727%
599835	0.9864	0.995	-0.865%
650200	0.9864	0.995	-0.869%

Table 9. Incompressible Flow Discharge Coefficient Values for 0.5  $\beta$  Classical Venturi.

$Re$	$C_{d\_INC}$	$C_{d\_INC}$ (Eq. 19)	% Dif
230023	0.9827	0.995	-1.239%
299308	0.9839	0.995	-1.113%
415021	0.9855	0.995	-0.957%
749967	0.9860	0.995	-0.908%
1050619	0.9864	0.995	-0.864%
1500192	0.9871	0.995	-0.797%
1600284	0.9871	0.995	-0.789%

Table 10. Incompressible Flow Discharge Coefficient Values for 0.6  $\beta$  Classical Venturi.

$Re$	$C_{d\_INC}$	$C_{d\_INC}$ (Eq. 19)	% Dif
229772	0.9850	0.995	-1.006%
599973	0.9855	0.995	-0.950%
1498284	0.9870	0.995	-0.807%
1597971	0.9878	0.995	-0.721%

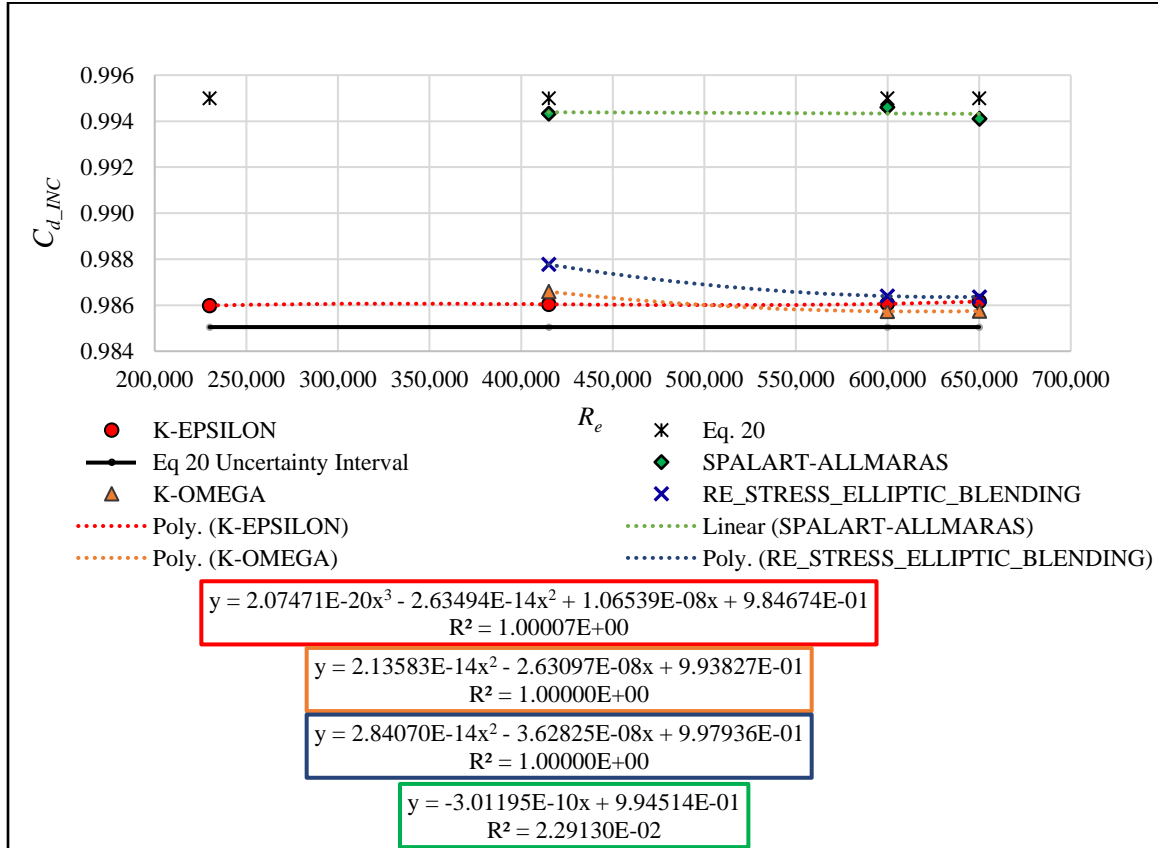


Figure 11. Incompressible Flow Discharge Coefficient Values and Trendline Equations for 0.4  $\beta$  Classical Venturi.

Classical Venturi incompressible flow simulations for all  $\beta$ 's, regardless of the selected turbulence model, consistently predict  $C_{d\_INC}$  values less than the theoretical  $C_{d\_INC}$ . A similar trend is observable for high  $Re$  ( $Re \geq 100,000$ ), Venturi  $C_{d\_INC}$  values predicted in Hollingshead et al.'s study. Hollingshead et al.'s study also used the Realizable K-Epsilon Two-Layer Turbulence Model (2011). This demonstrates commercially available turbulence models' tendency to overpredict the energy loss in an incompressible flow passing through a Classical Venturi. Interestingly, inspection of tables 5, 9, and 10 reveals when using the Realizable K-Epsilon Two-Layer Turbulence Model, the

agreement between computed  $C_{d\_INC}$  values and theoretical  $C_{d\_INC}$  values increases with increasing  $Re$ .

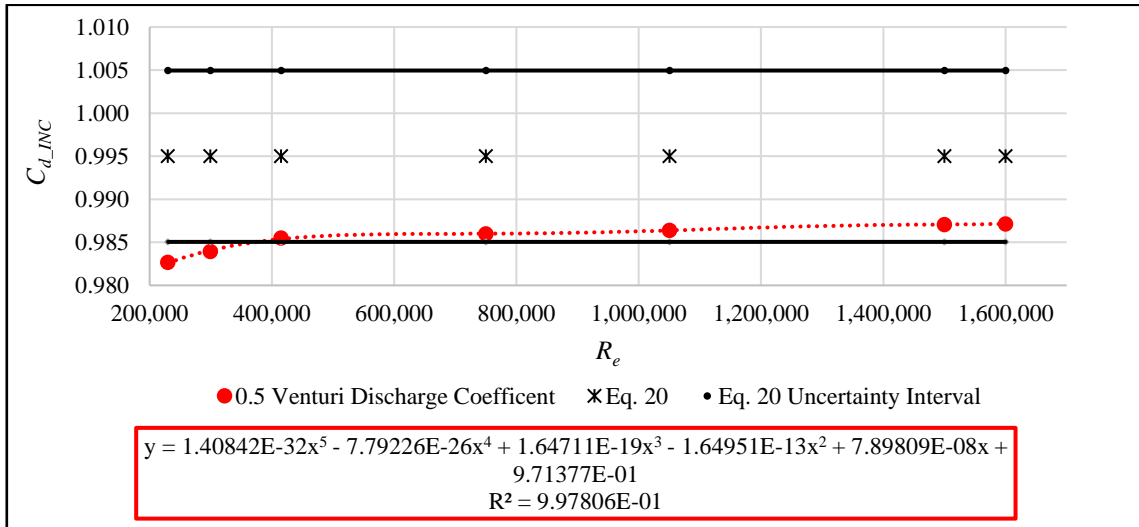


Figure 12. Incompressible Flow Discharge Coefficient Values and Trendline Equation for 0.5  $\beta$  Classical Venturi.

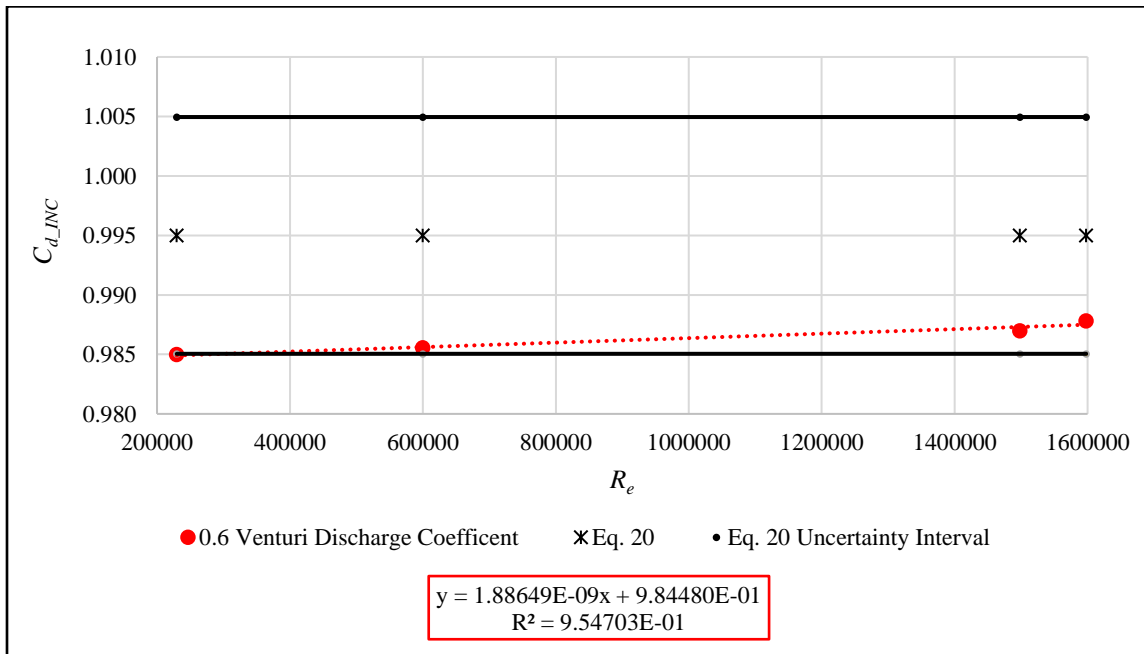


Figure 13. Incompressible Flow Discharge Coefficient Values and Trendline Equation for 0.6  $\beta$  Classical Venturi.

Remarkably, the  $C_{d\_INC}$  values computed using the Standard Spalart-Allmaras turbulence model had less than a 0.1% difference with the theoretical  $C_{d\_INC}$ . This supports Prassanna et al.'s finding of the Spalart-Allmaras turbulence model outperforming a variety of other turbulence models (K-omega standard, K-omega-SST and K- $\epsilon$ -standard) in the computation of accurate Venturi  $C_{d\_INC}$  values (2016). Prassanna et al. also used the agreement of computed  $C_{d\_INC}$  values with  $C_{d\_INC} = 0.995$  as an indicator of accuracy.

However, Prassanna et. al reliably computed  $C_{d\_INC}$  values with roughly a 1.0% difference with the theoretical  $C_{d\_INC}$  (2016). This is comparable to the magnitudes of differences calculated in this study using the Realizable K-Epsilon Two-Layer, SST(Menter) K-Omega, and Reynolds Stress Turbulence with Elliptic Blending turbulence models. Interestingly, CFD  $\epsilon$  values are relative to  $C_{d\_INC}$  values insensitive to the selected turbulence model. This claim is substantiated and reiterated in the following sections.

**Classical Venturi Compressible Flow Simulations.**  $C_{d\_CMP}$  values for 0.4, 0.5, and 0.6  $\beta$  Classical Venturi simulation are presented in this section (Tables 11-16, Figures 14-17). The relative uncertainty of  $\epsilon$  was calculated using Equation 21 (ASME 2007).

$$\text{Relative Uncertainty of Eq. 10} = \pm(4 + 100\beta^8) \left(1 - \frac{P_2}{P_1}\right) \quad (21)$$

Table 11. Gas Expansion Factors for  $0.4 \beta$  Classical Venturi Determined Using Realizable K-Epsilon Two-Layer Turbulence Model.

$Re$	$C_{d\_CMP}$	$P_2/P_1$	$\varepsilon$ CFD	$\varepsilon$ (Eq. 10)	% Dif
229727	0.9801	0.9731	0.9941	0.9938	0.0345%
416704	0.9650	0.9097	0.9788	0.9788	0.0019%
606174	0.9401	0.8027	0.9535	0.9528	0.0722%

Table 12. Gas Expansion Factors for  $0.4 \beta$  Classical Venturi Determined Using Standard Spalart-Allmaras Turbulence Model.

$Re$	$C_{d\_CMP}$	$P_2/P_1$	$\varepsilon$ CFD	$\varepsilon$ (Eq. 10)	% Dif
415672	0.9736	0.9110	0.9788	0.9792	-0.0371%
602741	0.9491	0.8051	0.9542	0.9538	0.0412%

Table 13. Gas Expansion Factors for  $0.4 \beta$  Classical Venturi Determined Using SST(Menter) K-Omega Turbulence Model.

$Re$	$C_{d\_CMP}$	$P_2/P_1$	$\varepsilon$ CFD	$\varepsilon$ (Eq. 10)	% Dif
417481	0.9655	0.9100	0.9787	0.9789	-0.0183%
608475	0.9399	0.8038	0.9535	0.9528	0.0688%

Table 14. Gas Expansion Factors for  $0.4 \beta$  Classical Venturi Determined Using Reynolds Stress Turbulence with Elliptic Blending Turbulence Model.

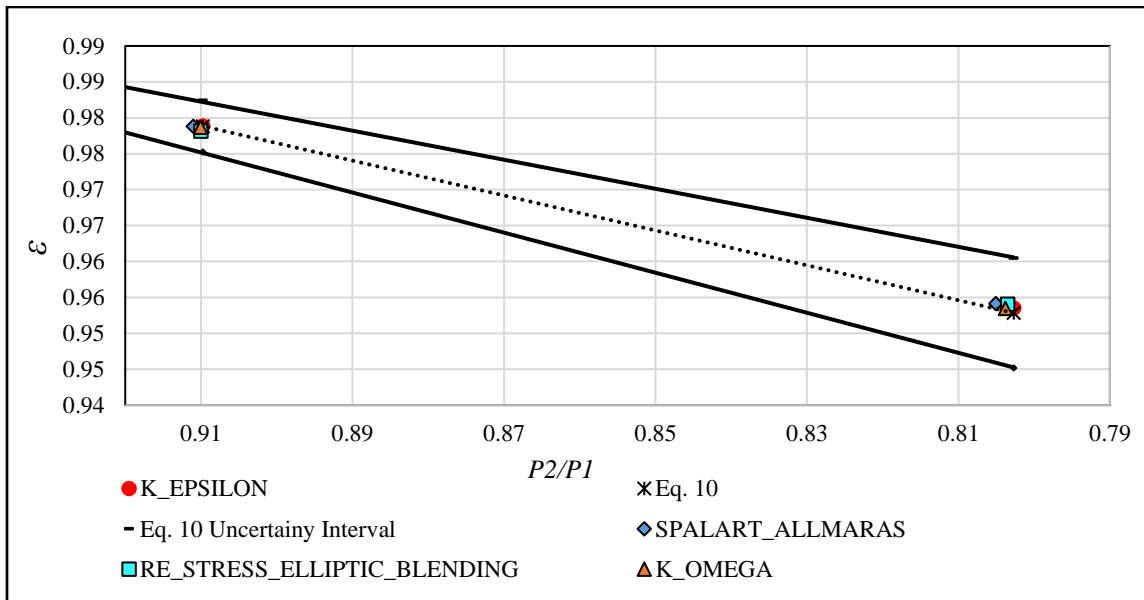
$Re$	$C_{d\_CMP}$	$P_2/P_1$	$\varepsilon$ CFD	$\varepsilon$ (Eq. 10)	% Dif
416949	0.9661	0.9100	0.9781	0.9789	-0.0761%
606697	0.9411	0.8035	0.9540	0.9529	0.1154%

Table 15. Gas Expansion Factors for  $0.5 \beta$  Classical Venturi.

$Re$	$C_{d\_CMP}$	$P_2/P_1$	$\varepsilon$ CFD	$\varepsilon$ (Eq. 10)	% Dif
229824	0.9801	0.9894	0.9974	0.9974	0.0032%
602226	0.9680	0.9259	0.9818	0.9818	-0.0024%
1514766	0.9350	0.8544	0.9472	0.9465	0.0755%

Table 16. Gas Expansion Factors for 0.6  $\beta$  Classical Venturi.

$Re$	$C_{d\_CMP}$	$P_2/P_1$	$\varepsilon$ CFD	$\varepsilon$ (Eq. 10)	% Dif
230486	0.9830	0.9952	0.9980	0.9987	0.0666%
600952	0.9770	0.9673	0.9913	0.9912	-0.0015%
1505564	0.9634	0.9385	0.9761	0.9756	-0.0214%

Figure 14. Gas Expansion Factors for 0.4  $\beta$  Classical Venturi Determined Using Various Turbulence Models.

Classical Venturi compressible flow simulations for all  $\beta$ 's, regardless of the selected turbulence model (Figure 14), consistently predicted  $\varepsilon$  values with roughly a 0.1% maximum difference with theoretical  $\varepsilon$  values. This demonstrates the relative insensitivity of  $\varepsilon$ , when compared to  $C_{d\_INC}$ , to the selected turbulence model. Other than supporting this study's modeling approach, this is an important finding for two reasons.

First, it agrees with Buckingham's observation that values of  $\varepsilon$  "... are much less sensitive to changes of tap location or roughness of the pipe than the value of  $K$ " (1932).

The variable  $K$  is equivalent to  $C_{d\_INC}$  in this study. If  $\varepsilon$  is relatively insensitive to turbulence producing processes, such as roughness, it makes sense that computed  $\varepsilon$  values would be relatively insensitive to the effects of turbulence predicted by a given turbulence model. The relative insensitivity of  $\varepsilon$  values to different Standard Concentric orifice plate tap locations described in the following sections.

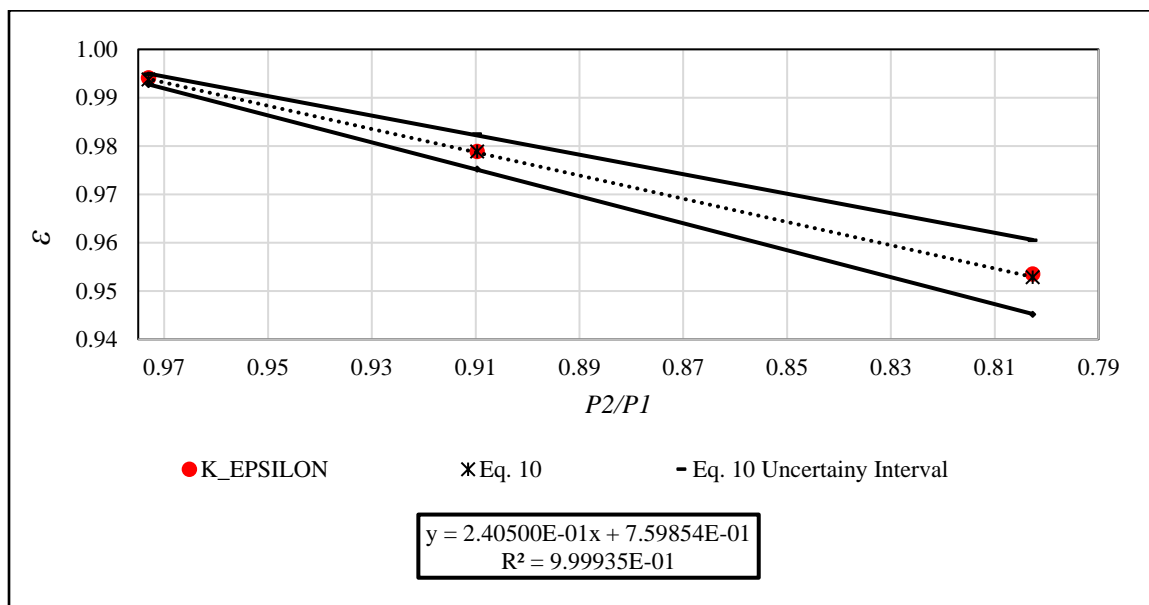


Figure 15. Gas Expansion Factors for  $0.4 \beta$  Classical Venturi Determined Using Realizable K-Epsilon Two-Layer Turbulence Model

Second, the inability of commercially available CFD software to accurately predict turbulence using relatively computationally efficient, semi-empirical turbulence models is commonly attributed as a source of error in expert modeling efforts (Versteeg and Malalasekera 2011). Given that the predicted  $\varepsilon$  values are relatively insensitive to the turbulence model used in their computation this indicates CFD  $\varepsilon$  values may be appropriate for applications requiring high accuracy flow measurements. However,  $\varepsilon$

equations produced from CFD data should not be implied as having the same accuracy and degree of certainty as  $\varepsilon$  equations produced from high quality laboratory data.

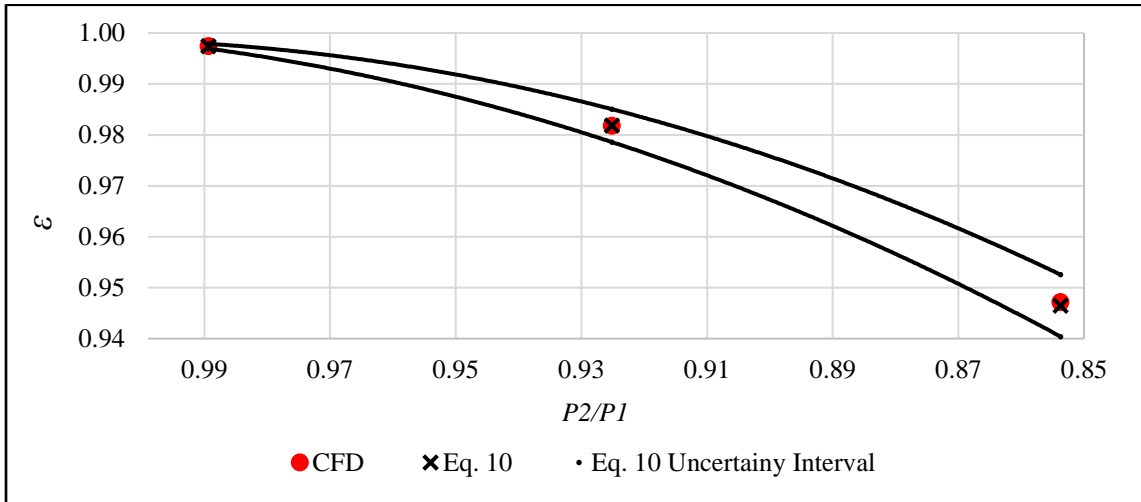


Figure 16. Gas Expansion Factors for 0.5  $\beta$  Classical Venturi

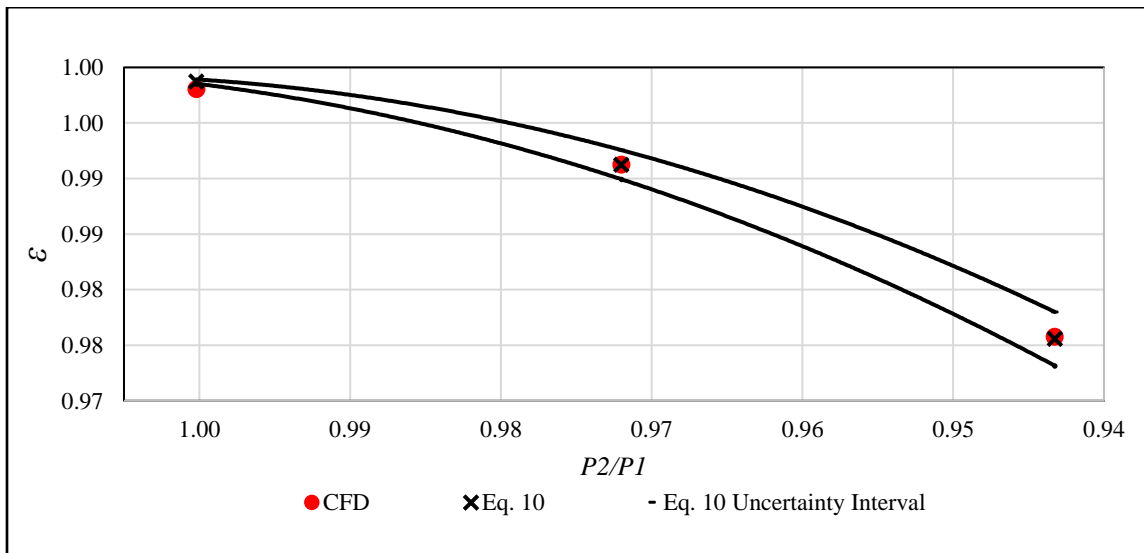


Figure 17. Gas Expansion Factors for 0.6  $\beta$  Classical Venturi

Finally, it is interesting to note that the linear trend of the 0.4  $\beta$  Venturi  $\varepsilon$  values differs from the convex shaped trend of the of the 0.5  $\beta$  and 0.6  $\beta$  Venturi trendlines. The tendency of  $\varepsilon$  to plot with a linear or slightly convex trends was also observed by

Buckingham (1932). Therefore, although  $\varepsilon$  typically plots as a linear function of  $P2/PI$ , it is important to remember this trend is not universal to all DPRM and  $\beta$  values.

### Standard Concentric Orifice Plate

In this section SC orifice plate simulation's  $C_{d\_INC}$  and  $\varepsilon$  values for  $\beta$  values of 0.4, 0.5, and 0.6 are presented. CFD  $C_{d\_INC}$  values calculated from simulation results were compared to theoretical  $C_{d\_INC}$  values predicted by the Reader-Harris/Gallagher (Equation 22) (ISO 2003). The relative uncertainty of Equation 22 for  $0.2 \leq \beta \leq 0.6$  is 0.5%, expressed at a 95% confidence interval. CFD  $\varepsilon$  values were compared against theoretical  $\varepsilon$  values predicted using Equations 13 and 14. The relative uncertainty, in percent, of  $\varepsilon$  is calculated using Equation 23 and 24 for Equations 13 and 14 respectively, expressed at a 95% confidence interval (ASME, 1985; ISO, 2003).

$$\begin{aligned}
 C_{d\_INC} = & 0.5961 + 0.0261\beta^2 - 0.216\beta^8 + 0.000521 \left( \frac{10^6 \beta}{R_e} \right)^{0.7} \\
 & + (0.0188 + 0.0063 A)\beta^{3.5} \left( \frac{10^6}{R_e} \right)^{0.3} \\
 & + (0.043 + 0.08e^{-10L_1} - 0.123e^{-7L_1})(1 - 0.11A) \frac{\beta^4}{1 - \beta^4} \\
 & - 0.031(\dot{M}_2 - 0.8\dot{M}_2^{1.1})\beta^{1.3}
 \end{aligned} \tag{22}$$

$$L_1 = l_1/D$$

$$\dot{L}_2 = \dot{l}_2/D$$

$$\dot{M}_2 = \frac{2\dot{L}_2}{1 - \beta}$$

$$A = \left( \frac{19000\beta}{Re} \right)^{0.8}$$

Where  $l_1$  is distance of the upstream tap from the upstream face of the orifice plate ( $l_1 = D$  for  $D$  and  $D/2$  taps,  $l_1 = 25.4$  mm for flange taps, and  $l_1 = 0$  for corner taps), and  $\dot{L}_2$  the distance of the downstream tap from the downstream face of the orifice plate ( $\dot{L}_2 = D/2$  for  $D$  and  $D/2$  taps and  $\dot{L}_2 = l_1$  for flange and corner taps).

$$\text{Relative Uncertainty of Eq. 13 (Buckingham Eq.)} = 4 \left( 1 - \frac{P_2}{P_1} \right) \% \quad (23)$$

$$\text{Relative Uncertainty of Eq 14 (ReaderHarris Eq.)} = \frac{3.5}{\kappa} \left( 1 - \frac{P_2}{P_1} \right) \% \quad (24)$$

### Standard Concentric Orifice Plate Incompressible Flow Simulations. $C_{d\_INC}$ SC

orifice plate simulations are presented in this section (Tables 17-19, Figures 18-20).

Table 17. Incompressible Flow Discharge Coefficients for 0.4  $\beta$  Standard Concentric Orifice Plate

$Re$	$D$ and $D/2$ Taps			Flange Taps			Corner Taps		
	$C_{d\_INC}$	$C_{d\_INC}$ (Eq. 20)	% Dif	$C_{d\_INC}$	$C_{d\_INC}$ (Eq. 20)	% Dif	$C_{d\_INC}$	$C_{d\_INC}$ (Eq. 20)	% Dif
229269	0.6032	0.6009	0.391%	0.6025	0.6016	0.148%	0.6025	0.6021	0.057%
331119	0.6027	0.6006	0.361%	0.6020	0.6013	0.117%	0.6020	0.6018	0.023%
428483	0.6024	0.6004	0.342%	0.6017	0.6011	0.091%	0.6016	0.6016	-0.003%
601797	0.6018	0.6002	0.277%	0.6010	0.6009	0.008%	0.6009	0.6014	-0.083%
699923	0.6016	0.6001	0.247%	0.6007	0.6008	-0.017%	0.6007	0.6013	-0.108%
876364	0.6014	0.6000	0.234%	0.6005	0.6007	-0.038%	0.6005	0.6012	-0.129%

For all SC orifice plate  $\beta$  values the predicted  $C_{d\_INC}$  values vary in accuracy depending on the tap set used.  $C_{d\_INC}$  values computed from  $D$  and  $D/2$  taps differ the most from the theoretical  $C_{d\_INC}$  values. Computed flange and corner tap  $C_{d\_INC}$  values are practically the same, and plot virtually on top of each other (Figures 18-20). This is reasonable because both tap sets fall within the stagnation zones upstream and downstream of the orifice plate. Therefore, velocity and pressure gradients between the flange and corner taps are negligible (Figures 21-22).

Table 18. Incompressible Flow Discharge Coefficients for 0.5  $\beta$  Standard Concentric Orifice Plate

$Re$	$D$ and $D/2$ Taps			Flange Taps			Corner Taps		
	$C_{d\_INC}$	$C_{d\_INC}$ (Eq. 20)	% Dif	$C_{d\_INC}$	$C_{d\_INC}$ (Eq. 20)	% Dif	$C_{d\_INC}$	$C_{d\_INC}$ (Eq. 20)	% Dif
229264	0.6083	0.6047	0.583%	0.6064	0.6048	0.262%	0.6063	0.6054	0.153%
331112	0.6075	0.6042	0.544%	0.6056	0.6043	0.224%	0.6056	0.6049	0.120%
499812	0.6068	0.6038	0.493%	0.6046	0.6038	0.133%	0.6046	0.6044	0.026%
701510	0.6061	0.6035	0.433%	0.6036	0.6035	0.021%	0.6036	0.6041	-0.078%
801261	0.6058	0.6034	0.396%	0.6034	0.6034	-0.003%	0.6034	0.6040	-0.102%
1149642	0.6053	0.6031	0.363%	0.6029	0.6031	-0.036%	0.6029	0.6037	-0.139%

Table 19. Incompressible Flow Discharge Coefficients for 0.6  $\beta$  Standard Concentric Orifice Plate

$Re$	$D$ and $D/2$ Taps			Flange Taps			Corner Taps		
	$C_{d\_INC}$	$C_{d\_INC}$ (Eq. 20)	% Dif	$C_{d\_INC}$	$C_{d\_INC}$ (Eq. 20)	% Dif	$C_{d\_INC}$	$C_{d\_INC}$ (Eq. 20)	% Dif
229,269	0.6138	0.6095	0.699%	0.6096	0.6075	0.350%	0.6095	0.6079	0.252%
500,071	0.6116	0.6080	0.584%	0.6066	0.6060	0.095%	0.6065	0.6064	0.014%
801,745	0.6102	0.6073	0.473%	0.6050	0.6053	-0.047%	0.6050	0.6057	-0.122%
1,149,644	0.6095	0.6069	0.437%	0.6042	0.6048	-0.102%	0.6042	0.6052	-0.179%

Interestingly, in a trend that is directly opposite to the one observed with the Classical Venturi, when considering  $D$  and  $D/2$  tap data, the computed  $C_{d\_INC}$  values are greater

than theoretical  $C_{d\_INC}$  values. Therefore, if only considering  $D$  and  $D/2$  data, it could be inferred CFD routinely under predicts the energy loss and overpredicts the flow rate of an incompressible flow at given  $Re$  passing through a SC orifice plate. However, when considering flange and corner tap data it can be inferred CFD tends to under predict the energy loss and over predict flow rate at lower values of  $Re$  until a  $Re$  of approximately 600,000.

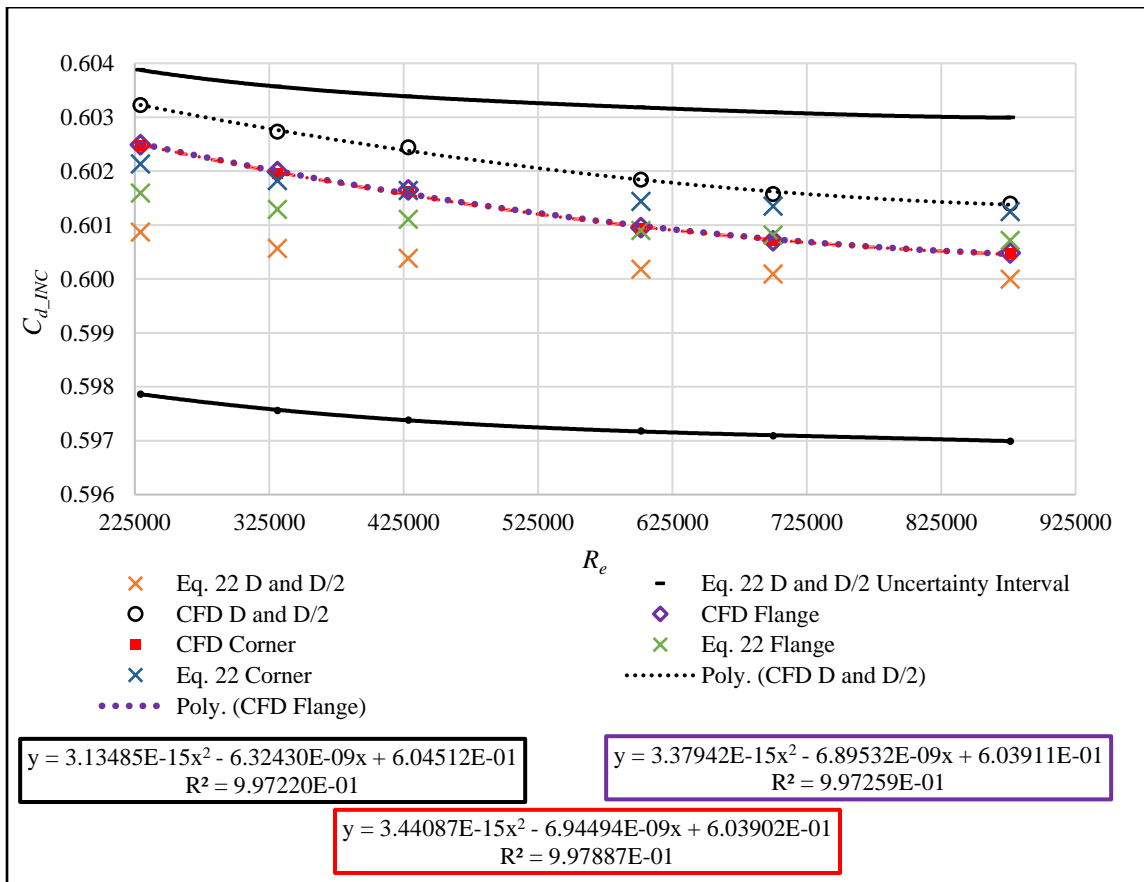


Figure 18. Incompressible Flow Discharge Coefficient Values for 0.4  $\beta$  Standard Concentric Orifice Plate.

Past  $Re \approx 600,000$  the trend reverses and energy loss is overpredicted and flow rate underpredicted. Considering the discrepancies in first the accuracy of  $C_{d\_INC}$  determined

from the different tap sets, and second the over or underprediction of energy loss and flow rate, it is surprising that the tap location in SC orifice plate has relatively little impact on the  $\epsilon$  value calculated using the different tap sets' data.

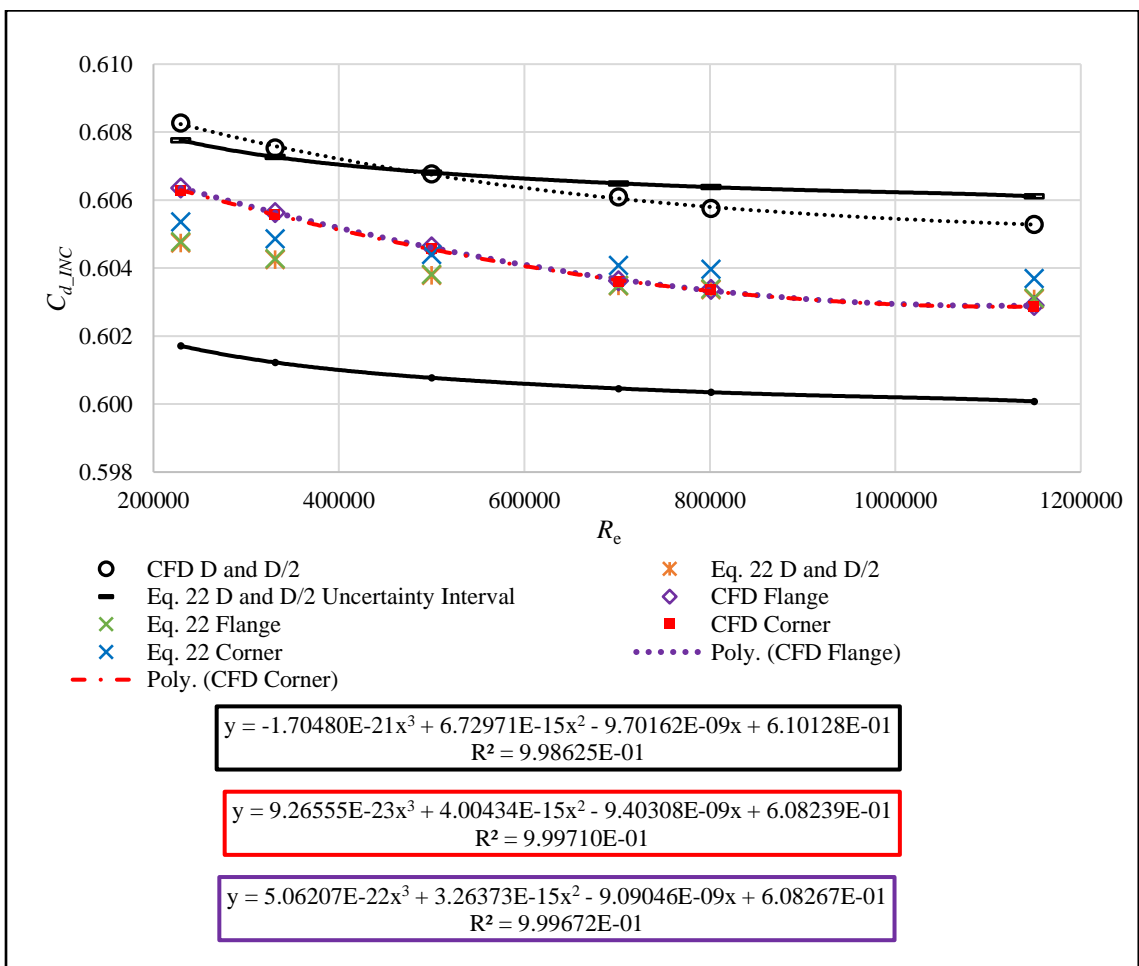


Figure 19. Incompressible Flow Discharge Coefficient Values for 0.5  $\beta$  Standard Concentric Orifice Plate.

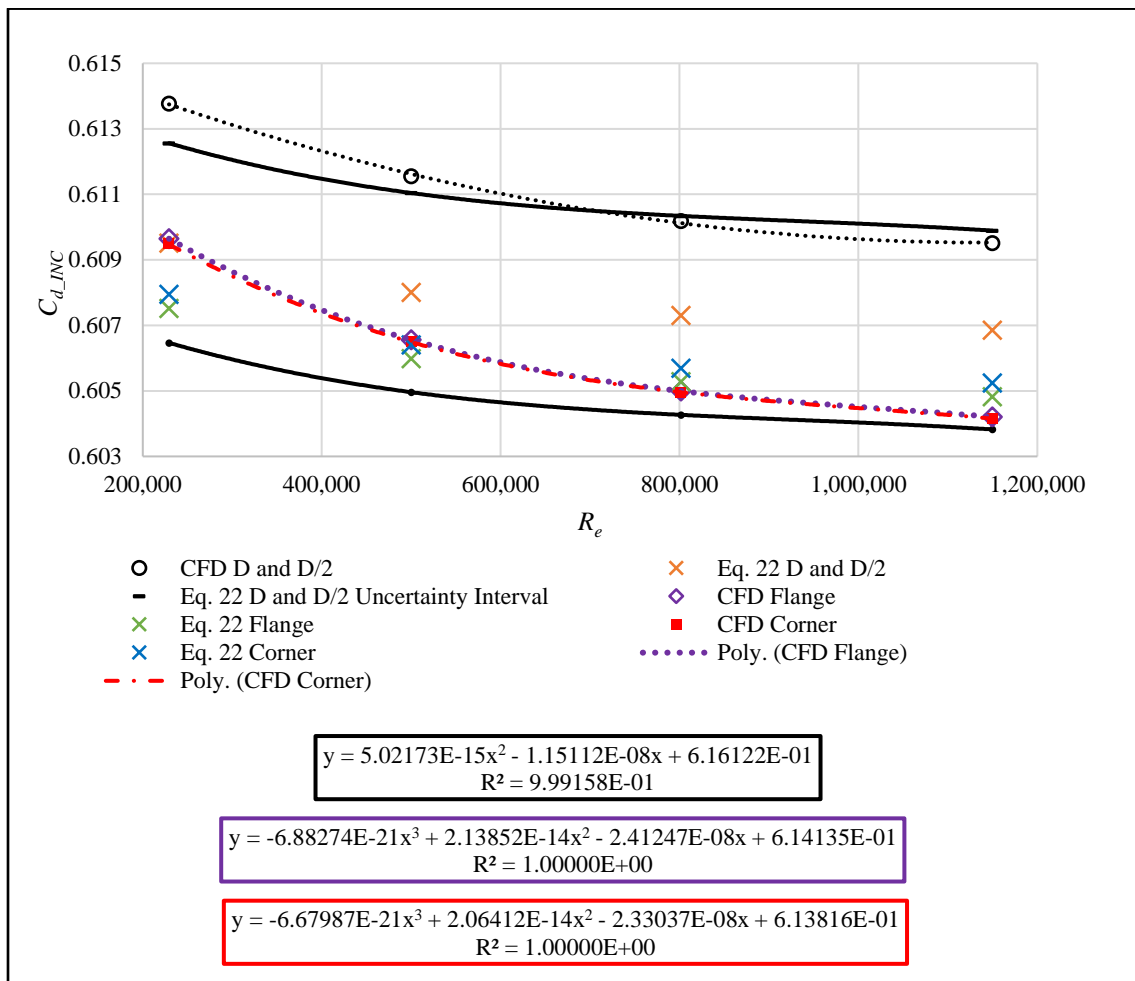


Figure 20. Incompressible Flow Discharge Coefficient Values for 0.6  $\beta$  Standard Concentric Orifice Plate.

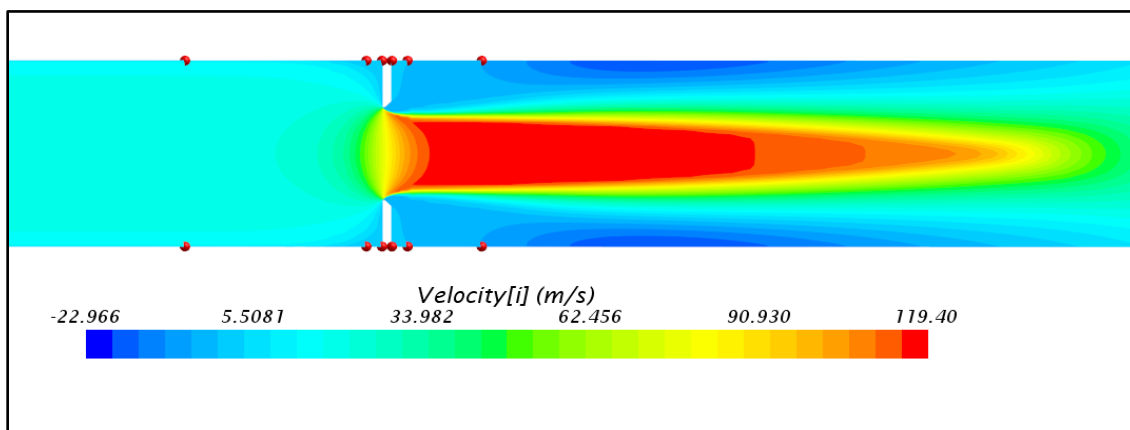


Figure 21. Standard Concentric Orifice Plate Velocity Scene Showing Pressure Taps

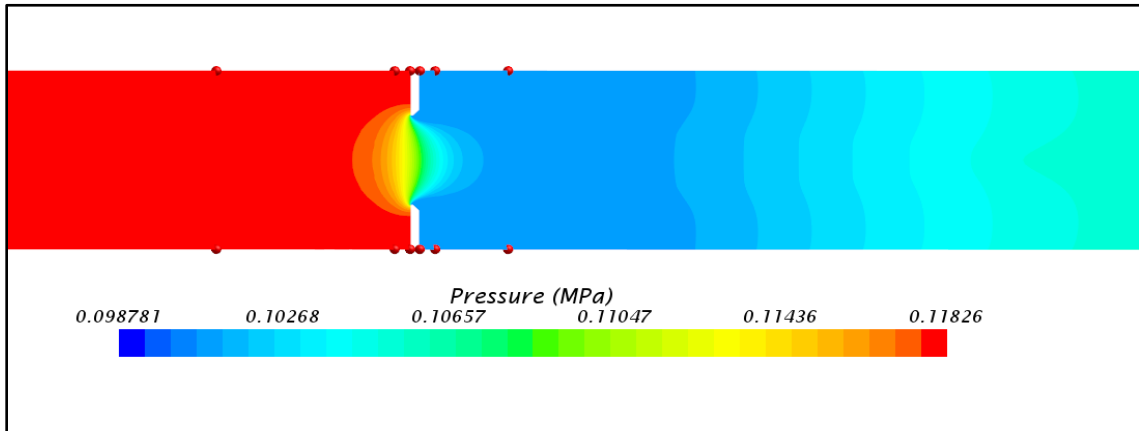


Figure 22. Standard Concentric Orifice Plate Pressure Scene Showing Pressure Taps

**Standard Concentric Orifice Plate Compressible Flow Simulations.** SC orifice plate simulations predicted  $\varepsilon$  values are presented in this section (Tables 20-22, Figures 23-25). It is important to note that in Figures 23-25 the theoretical  $\varepsilon$  values calculated using Equation 13 and 14 and the Equation 14 uncertainty intervals are only representative of  $D$  and  $D/2$  taps. Therefore, the agreement of computed flange and corner  $\varepsilon$  values with the respective theoretical  $\varepsilon$  values calculated using Equation 14 is better than what might be assumed upon inspection of Figures 23-25.

For  $0.4 \beta$  SC orifice plate simulations, marginally better agreement of computed  $\varepsilon$  values and  $\varepsilon_{RH}$  values was obtained using  $D$  and  $D/2$  taps when compared to corner and flange taps. This is somewhat unexpected because for  $0.5$  and  $0.6 \beta$ 's the differences between computed  $\varepsilon$  values and  $\varepsilon_{RH}$  values were similar regardless of the taps used. It is also interesting to note that flange and corner taps consistently predicted higher  $\varepsilon$  values and, therefore, expansion effects than  $D$  and  $D/2$  taps at  $Re \approx 230000$ . Finally, all SC orifice plate compressible flow simulation's predicted  $\varepsilon$  values which agreed better with  $\varepsilon_{RH}$

values than  $\varepsilon$  values predicted using Equation 13, thereby supporting the widely accepted use of Equation 14 to predict  $\varepsilon$  values.

Table 20. Gas Expansion Factors for 0.4  $\beta$  Standard Concentric Orifice Plate

<i>D</i> and <i>D/2</i> Taps							
$Re$	$C_{d\_CMP}$	$P_2/P_1$	$\varepsilon$ CFD	$\varepsilon$ (Eq. 13)	$\varepsilon$ (Eq. 14)	%Dif (Eq. 13)	%Dif (Eq. 14)
234685	0.6000	0.9791	0.9948	0.9937	0.9946	0.105%	0.015%
545335	0.5858	0.8971	0.9730	0.9692	0.9733	0.391%	-0.028%
855405	0.5661	0.7824	0.9413	0.9349	0.9424	0.685%	-0.120%
Flange Taps							
234685	0.5993	0.9790	0.9936	0.9937	0.9946	-0.015%	-0.105%
545335	0.5849	0.8969	0.9716	0.9691	0.9732	0.252%	-0.167%
855405	0.5652	0.7820	0.9398	0.9347	0.9423	0.538%	-0.267%
Corner Taps							
234685	0.5993	0.9790	0.9935	0.9937	0.9946	-0.020%	-0.110%
545335	0.5849	0.8969	0.9715	0.9691	0.9732	0.249%	-0.171%
855405	0.5652	0.7820	0.9397	0.9347	0.9423	0.536%	-0.269%

Table 21. Gas Expansion Factors for 0.5  $\beta$  Standard Concentric Orifice Plate

<i>D</i> and <i>D/2</i> Taps							
$Re$	$C_{d\_CMP}$	$P_2/P_1$	$\varepsilon$ CFD	$\varepsilon$ (Eq. 13)	$\varepsilon$ (Eq. 14)	%Dif (Eq. 13)	%Dif (Eq. 14)
230894	0.6069	0.9920	0.9978	0.9975	0.9979	0.027%	-0.008%
744159	0.5929	0.9218	0.9785	0.9759	0.9791	0.268%	-0.058%
1143814	0.5769	0.8317	0.9531	0.9481	0.9543	0.529%	-0.125%
Flange Taps							
230894	0.6050	0.9920	0.9977	0.9975	0.9979	0.019%	-0.016%
744159	0.5906	0.9213	0.9785	0.9757	0.9789	0.287%	-0.040%
1143814	0.5745	0.8307	0.9528	0.9478	0.9540	0.536%	-0.121%
Corner Taps							
230894	0.6048	0.9920	0.9976	0.9975	0.9979	0.011%	-0.024%
744159	0.5905	0.9213	0.9785	0.9757	0.9789	0.287%	-0.041%
1143814	0.5744	0.8307	0.9528	0.9478	0.9540	0.535%	-0.122%

Table 22. Gas Expansion Factors for 0.6  $\beta$  Standard Concentric Orifice Plate

<i>D</i> and <i>D/2</i> Taps							
$Re$	$C_{d\_CMP}$	$P_2/P_1$	$\varepsilon$ CFD	$\varepsilon$ (Eq. 13)	$\varepsilon$ (Eq. 14)	%Dif (Eq. 13)	%Dif (Eq. 14)
229,527	0.6129	0.9965	0.9987	0.9989	0.9990	-0.020%	-0.034%
716,600	0.6046	0.9664	0.9904	0.9891	0.9903	0.135%	0.005%
1,047,901	0.5973	0.9297	0.9798	0.9771	0.9797	0.275%	0.011%
Flange Taps							
229,527	0.6087	0.9965	0.9984	0.9988	0.9990	-0.042%	-0.056%
716,600	0.5994	0.9658	0.9903	0.9889	0.9902	0.142%	0.010%
1,047,901	0.5921	0.9287	0.9796	0.9768	0.9794	0.284%	0.017%
Corner Taps							
229,527	0.6084	0.9965	0.9983	0.9988	0.9990	-0.057%	-0.071%
716,600	0.5993	0.9658	0.9902	0.9889	0.9902	0.136%	0.004%
1,047,901	0.5920	0.9287	0.9795	0.9768	0.9794	0.277%	0.010%

Regardless of the trends in  $\varepsilon$  values predicted using different tap configurations, the differences between computed  $\varepsilon$  values and  $\varepsilon_{RH}$  values are minute. Therefore, the capability of CFD to predict  $\varepsilon$  values with remarkable accuracy has been demonstrated for both Classical Venturi and SC orifice plate DPFM geometries. This provides additional support of this study's modeling approach, and, generally indicates CFD is an appropriate tool for determining  $\varepsilon$  values for DPFM geometries for which  $\varepsilon$  equations currently do not exist, such as wedge meters.

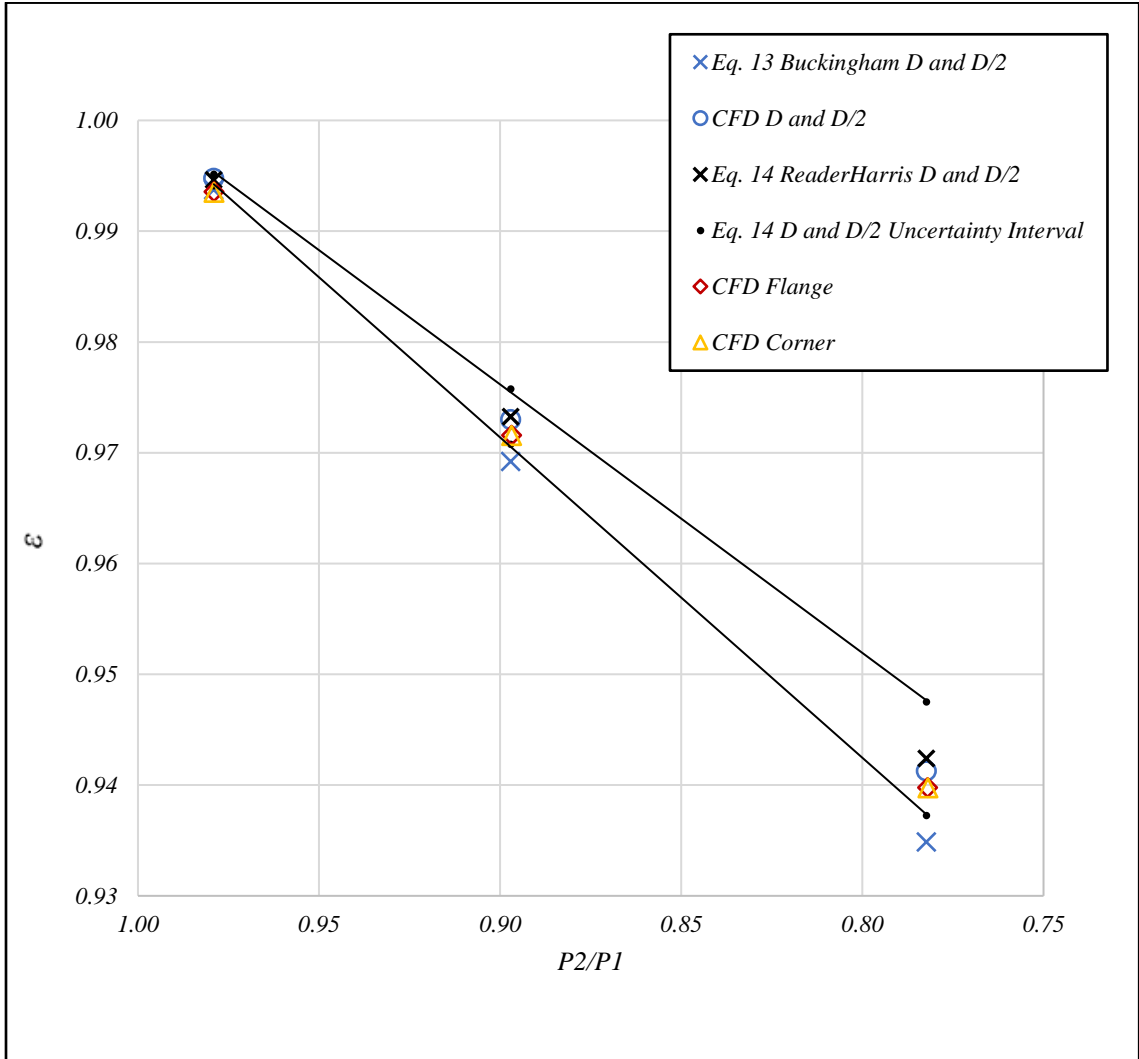


Figure 23. Gas Expansion Factors for 0.4  $\beta$  Standard Concentric Orifice Plate

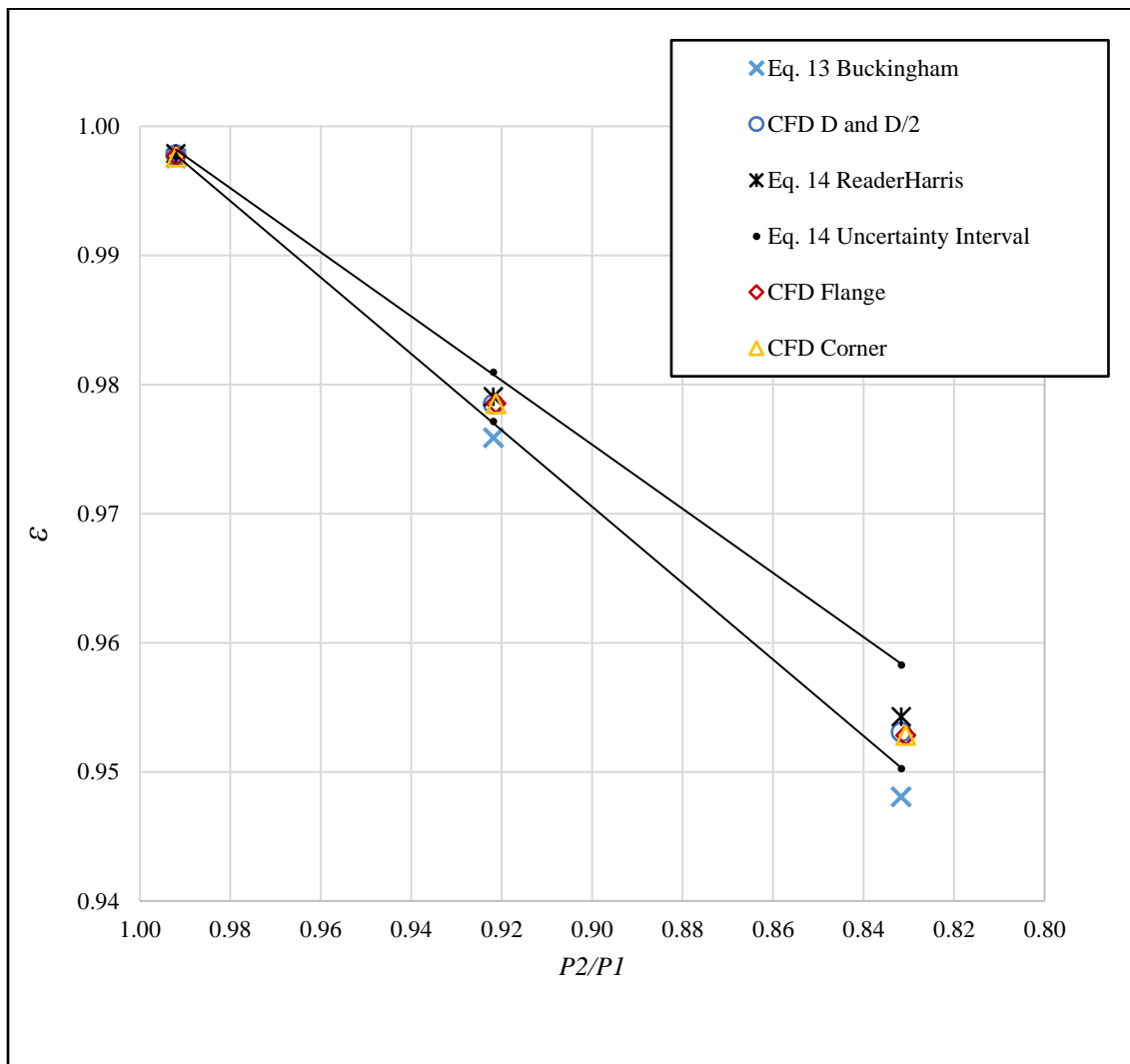


Figure 24. Gas Expansion Factors for 0.5  $\beta$  Standard Concentric Orifice Plate

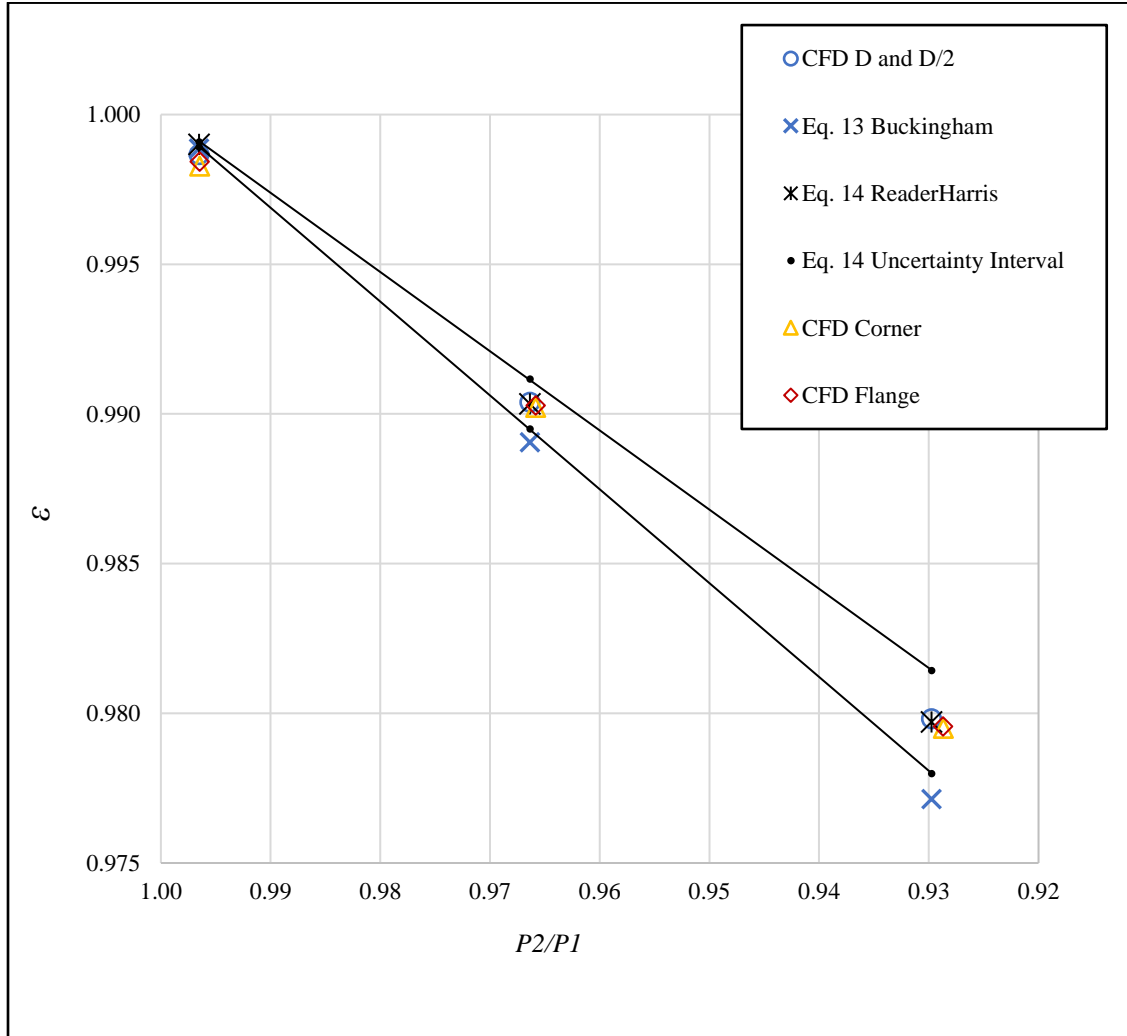


Figure 25. Gas Expansion Factors for 0.6  $\beta$  Standard Concentric Orifice Plate

## Wedge Meter

In this section wedge meter simulations'  $C_{d\_INC}$  and  $\epsilon$  values for  $\beta$ 's of 0.3789, 0.5019, and 0.6107 are presented. CFD  $C_{d\_INC}$  values calculated from simulation results were compared to the  $C_{d\_INC}$  values predicted by *ISO standard 1567:6-2019* (Equation 23) (2019). The relative uncertainty of Equation 23 for  $0.377 \leq \beta \leq 0.791$  is 4%, expressed at a 95% confidence interval. CFD  $\epsilon$  values were compared against  $\epsilon$  values predicted

using Equation 10. ISO standard 1567:6-2019 recommends the use of Equation 10 as an estimate for wedge meter  $\varepsilon$  values (2019).

$$C_{d_{INC}} = 0.77 - 0.09\beta \quad (25)$$

**Wedge Meter Incompressible Flow Simulations.**  $C_{d_{INC}}$  values from wedge meter simulations are presented in this section (Tables 23-25 and Figures 26-28).

Table 23. Incompressible Flow Discharge Coefficient Values for 0.3789  $\beta$  Wedge Meter

$Re$	$C_{d_{INC}}$	$C_{d_{INC}}$ (Eq. 25)	% Dif
230204	0.7422	0.7359	0.856%
250554	0.7424	0.7359	0.896%
330339	0.7438	0.7359	1.082%
430405	0.7443	0.7359	1.146%
500382	0.7455	0.7359	1.311%
701628	0.7465	0.7358	1.450%
1103076	0.7476	0.7358	1.604%

Table 24. Incompressible Flow Discharge Coefficient Values for 0.5019  $\beta$  Wedge Meter

$Re$	$C_{d_{INC}}$	$C_{d_{INC}}$ (Eq. 25)	% Dif
229775	0.7305	0.7248	0.779%
330885	0.7308	0.7248	0.824%
500263	0.7318	0.7248	0.963%
1102927	0.7326	0.7247	1.078%

Overall, wedge meter predicted  $C_{d_{INC}}$  values were surprisingly close to theoretical  $C_{d_{INC}}$  values for all  $\beta$  values. Considering Equation 25 has a relative uncertainty of 4% at a 95% confidence interval, the difference between computed and theoretical  $C_{d_{INC}}$  values is less useful as an indication of simulation accuracy when compared to Venturi

and SC orifice plate theoretical equations. In addition, “ISO 1567:2019” does not specify if Equation 25 was regressed from empirical data of single or various wedge tip geometries. Equation 25 is only defined as being limited in application to  $R_w \leq 1 \text{ mm}$ .  $R_w$  significantly impacts  $C_{d\_INC}$  values (Banchhor 2004). Therefore, the difference between predicted and theoretical  $C_{d\_INC}$  values may be at least partially due to all wedge geometries having a  $R_w$  of 1 mm.

Table 25. Incompressible Flow Discharge Coefficient Values for 0.6107  $\beta$  Wedge Meter

$R_e$	$C_{d\_INC}$	$C_{d\_INC}$ (Eq. 25)	% Dif
230165	0.71500	0.71497	0.004%
330968	0.71519	0.71497	0.030%
500304	0.71522	0.71497	0.035%
1102890	0.71589	0.71495	0.131%
1499745	0.71894	0.71502	0.549%

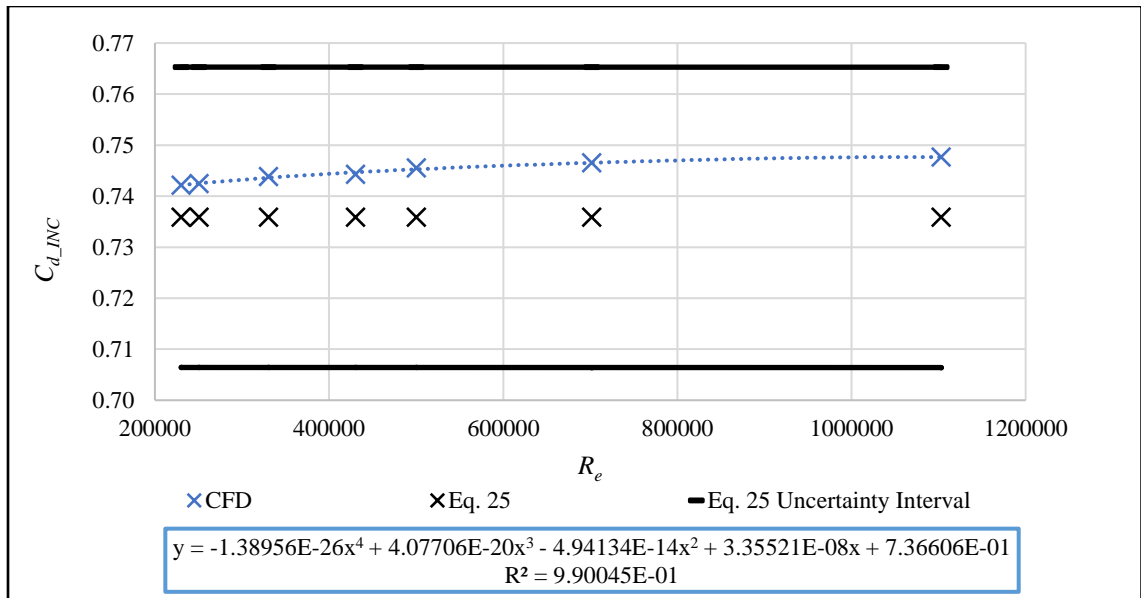


Figure 26. Incompressible Flow Discharge Coefficient Values for 0.3789  $\beta$  Wedge Meter

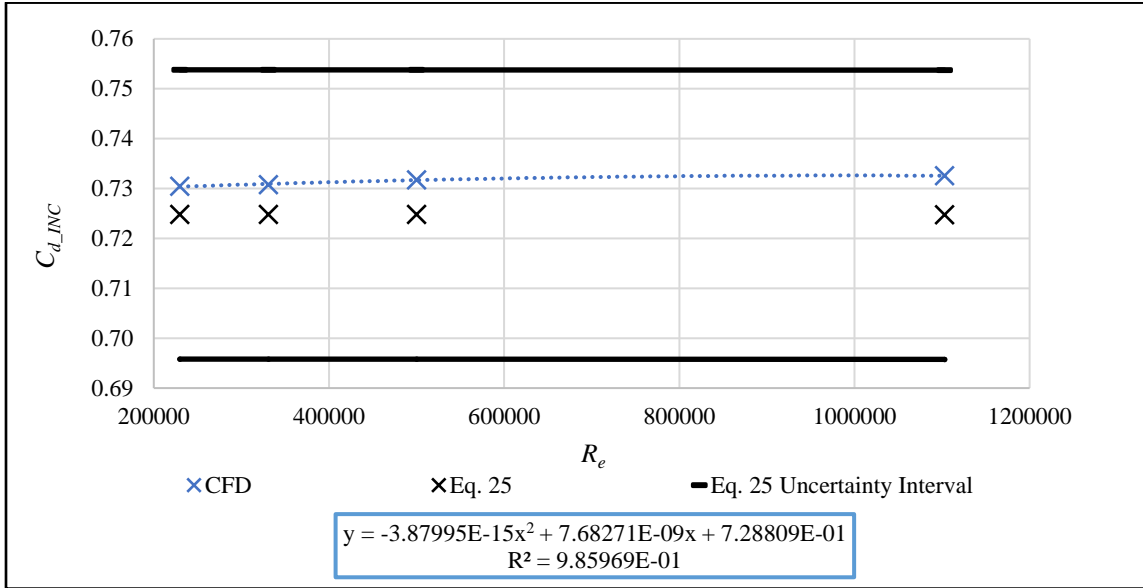


Figure 27. Incompressible Flow Discharge Coefficient Values for 0.5019  $\beta$  Wedge Meter

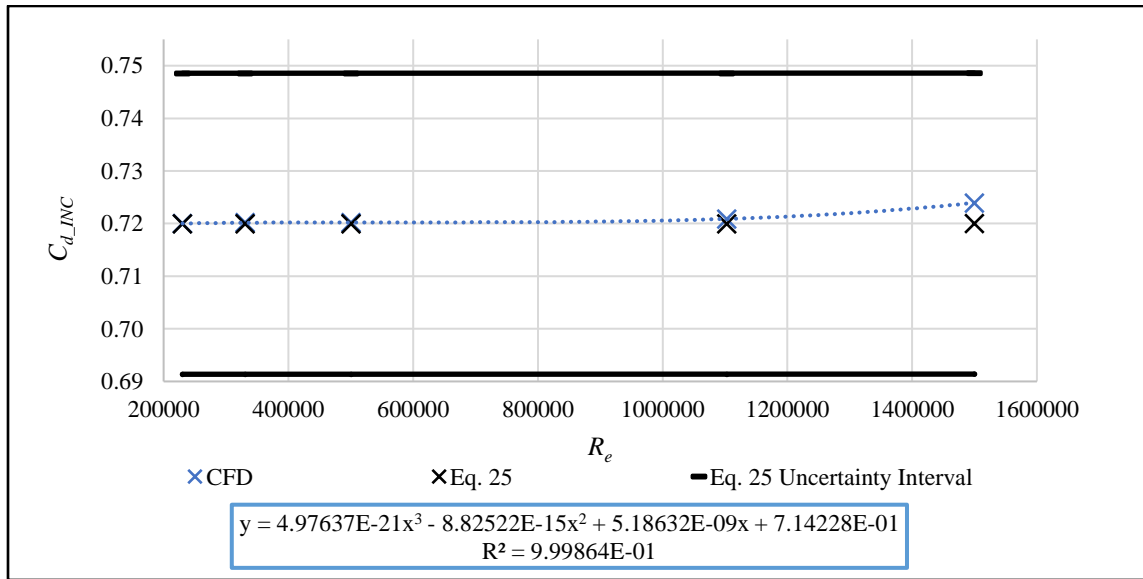


Figure 28. Incompressible Flow Discharge Coefficient Values for 0.6107  $\beta$  Wedge Meter

However, the sensitivity of  $C_{d\_INC}$  to  $R_w$  seems to lessen with increasing  $\beta$  values. The wedge simulations with  $\beta$  values of 0.6107 predict  $C_{d\_INC}$  values which agree extremely well with theoretical values until  $R_e \approx 1.1 \times 10^6$ . In addition, wedge meter simulations

with  $\beta$  values of 0.5019 predicted  $C_{d\_INC}$  values which agree better with theoretical  $C_{d\_INC}$  values than the 0.3789  $\beta$  simulations.

Considering predicted wedge  $C_{d\_INC}$  values for  $\beta$  values of 0.3789 and 0.5019 are relatively constant at high  $Re$  values, it is surprising predicted  $C_{d\_INC}$  values vary the most in 0.6107  $\beta$  simulations at high  $Re$  values. This indicates the 0.6107  $\beta$  simulation for  $Re \geq 1.1 \times 10^6$  is relatively flawed, when compared to lower  $Re$  simulations, despite the acceptable GCI value mesh refinements of the simulation produced. Ultimately, simulation results can be considered as sufficiently accurate due to  $\varepsilon$ 's relative insensitivity to small errors in  $C_{d\_INC}$  values.

**Wedge Meter Compressible Flow Simulations.**  $\varepsilon$  values from wedge meter simulations are presented in this section (Tables 26-29, Figures 29-31).

Table 26. Gas Expansion Factors for 0.3789  $\beta$  Wedge Meter

$Re$	$C_{d\_CMP}$	$P_2/P_1$	$\varepsilon$ CFD	$\varepsilon$ (Eq. 10)	% Dif
233632	0.738	0.983	0.994	0.990	0.34%
339505	0.732	0.964	0.984	0.980	0.43%
453268	0.727	0.938	0.976	0.965	1.09%
538689	0.723	0.915	0.970	0.952	1.87%
824872	0.694	0.818	0.929	0.895	3.75%

Table 27. Gas Expansion Factors for 0.5019  $\beta$  Wedge Meter

$Re$	$C_{d\_CMP}$	$P_2/P_1$	$\varepsilon$ CFD	$\varepsilon$ (Eq. 10)	% Dif
231167	0.731	0.995	1.000	0.997	0.36%
510159	0.725	0.974	0.990	0.985	0.60%
724599	0.718	0.948	0.981	0.969	1.21%
958779	0.710	0.911	0.968	0.947	2.23%

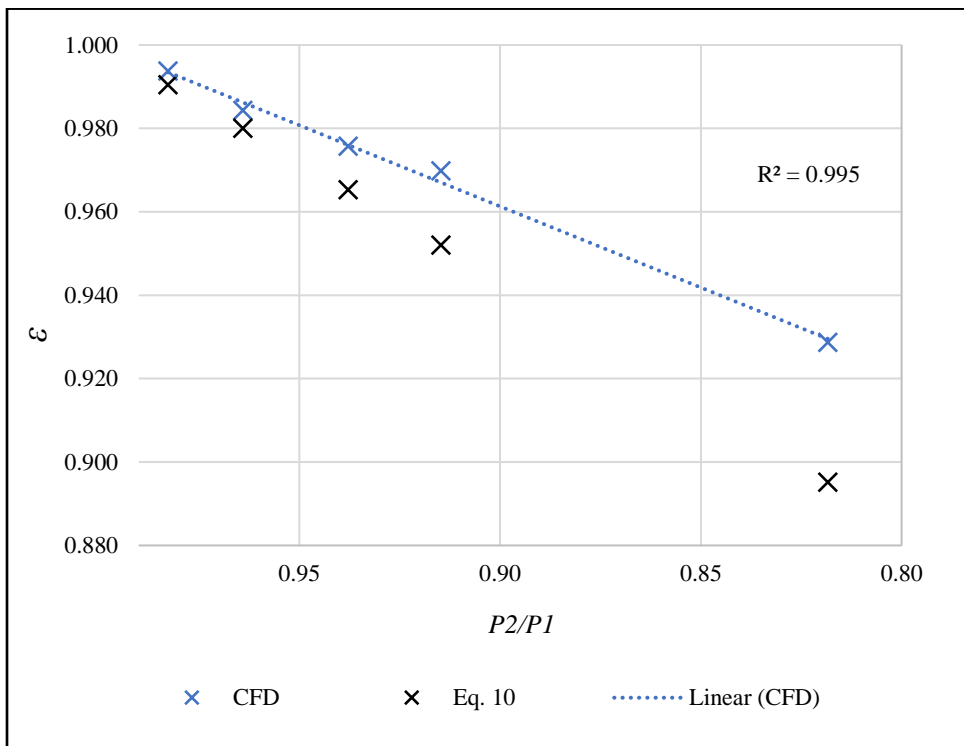
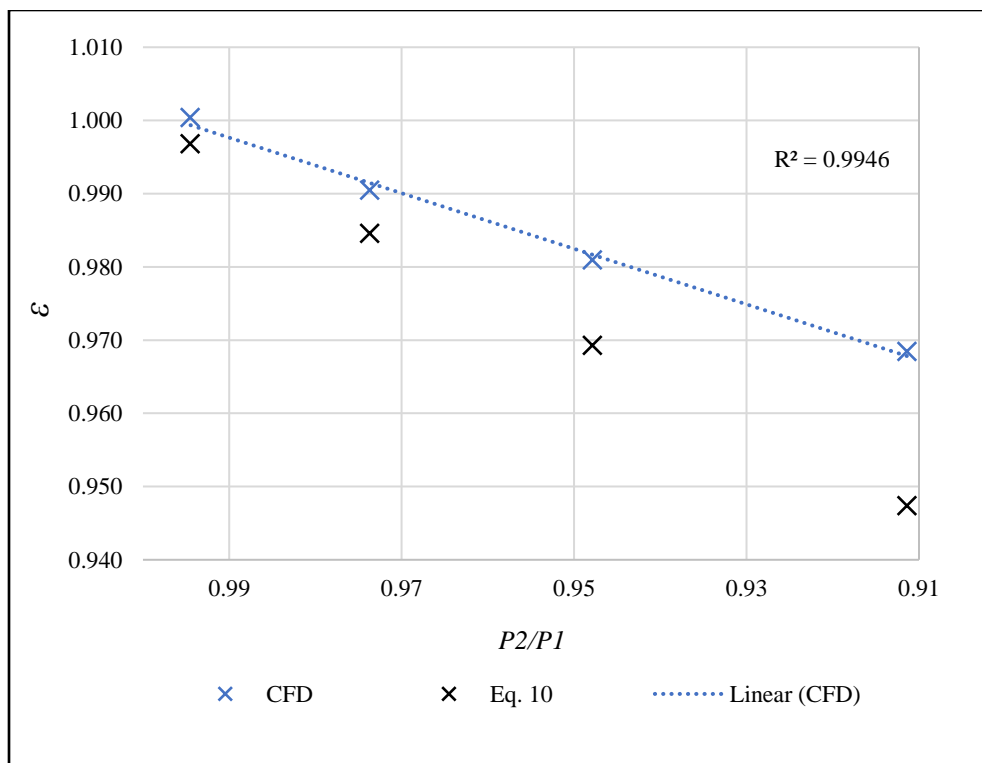
Table 28. Gas Expansion Factors for 0.6107  $\beta$  Wedge Meter

$Re$	$C_{d\_CMP}$	$P_2/P_1$	$\varepsilon$ CFD	$\varepsilon$ (Eq. 10)	% Dif
331400	0.714	0.995	0.998	0.997	0.14%
920014	0.704	0.962	0.984	0.975	0.91%
1265047	0.697	0.930	0.973	0.954	1.93%
1486816	0.691	0.904	0.961	0.937	2.54%

The modeling approach used to predict wedge  $\varepsilon$  equations has been shown to be appropriate based on Classical Venturi, and SC orifice plate simulation results. Therefore, it is reasonable to assume the wedge meter CFD  $\varepsilon$  values produced in this study are more accurate than those predicted by Equation 10. This is especially true at high pressure differentials. One way to assess the validity of this study's wedge  $\varepsilon$  values, for certain  $\beta$  and  $P_2/P_1$  values, is by plotting the wedge  $\varepsilon$  values alongside  $\varepsilon$  values predicted by existing  $\varepsilon$  equations for Classical Venturis, SC orifice plates, and cone meters (Figure 32). The cone meter  $\varepsilon$  values were calculated using Equation 26 (Stewart et. al 2001).

$$\varepsilon = 1 - (0.649 + 0.696\beta^4) \left(1 - \frac{P_2}{P_1}\right) \frac{1}{\kappa} \quad (26)$$

Wedge meter  $\varepsilon$  values plot between cone and SC orifice plate  $\varepsilon$  values. This makes sense considering cone meters have a  $C_{d\_INC}$  approximately equal to 0.8, wedge meters have a  $C_{d\_INC}$  approximately equal to 0.72, and SC orifice plates have a  $C_{d\_INC}$  approximately equal to 0.61. Therefore, the efficiency with which a given DPFM passes incompressible flows can be used to predict the relative magnitudes of its  $\varepsilon$  values in comparison to DPFMs with know  $\varepsilon$  values.

Figure 29. Gas Expansion Factors for  $0.3789 \beta$  Wedge MeterFigure 30. Gas Expansion Factors for  $0.5019 \beta$  Wedge Meter

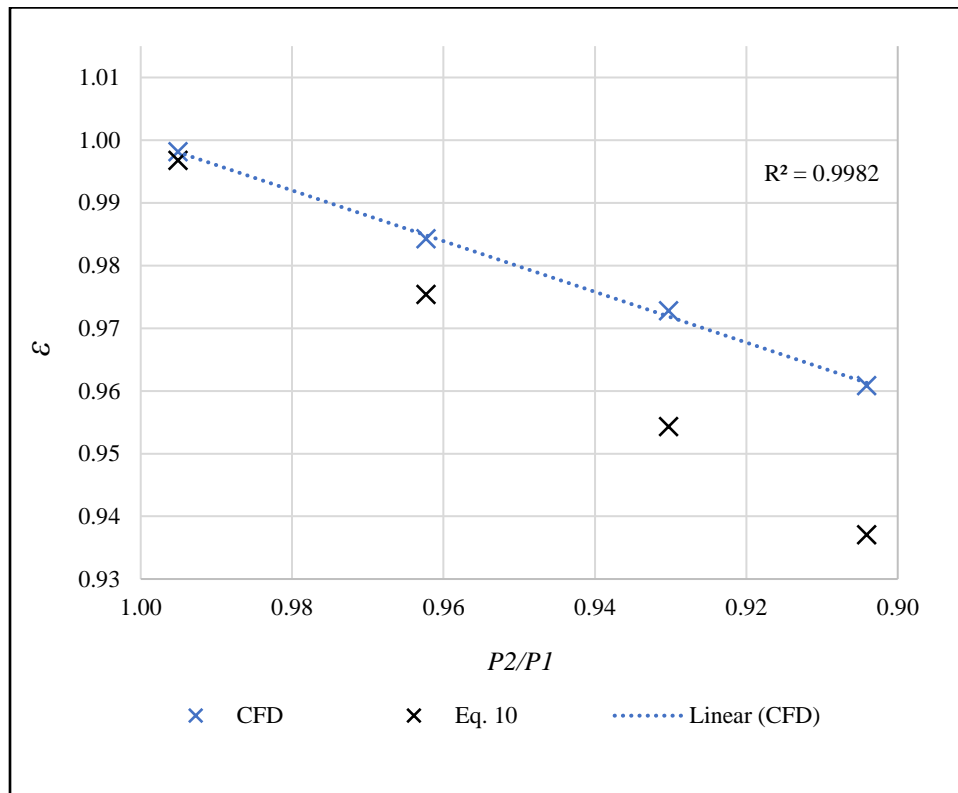


Figure 31. Gas Expansion Factors for 0.6107  $\beta$  Wedge Meter

Ultimately, this study's Classical Venturi, SC orifice plate, and wedge meter  $\epsilon$  data indicates this study's modeling approach can be used to produce  $\epsilon$  data acceptable for use in the regression of accurate empirical  $\epsilon$  equations for DPFMs, restricted to flow conditions where the ideal gas law is an appropriate assumption of gas behavior.

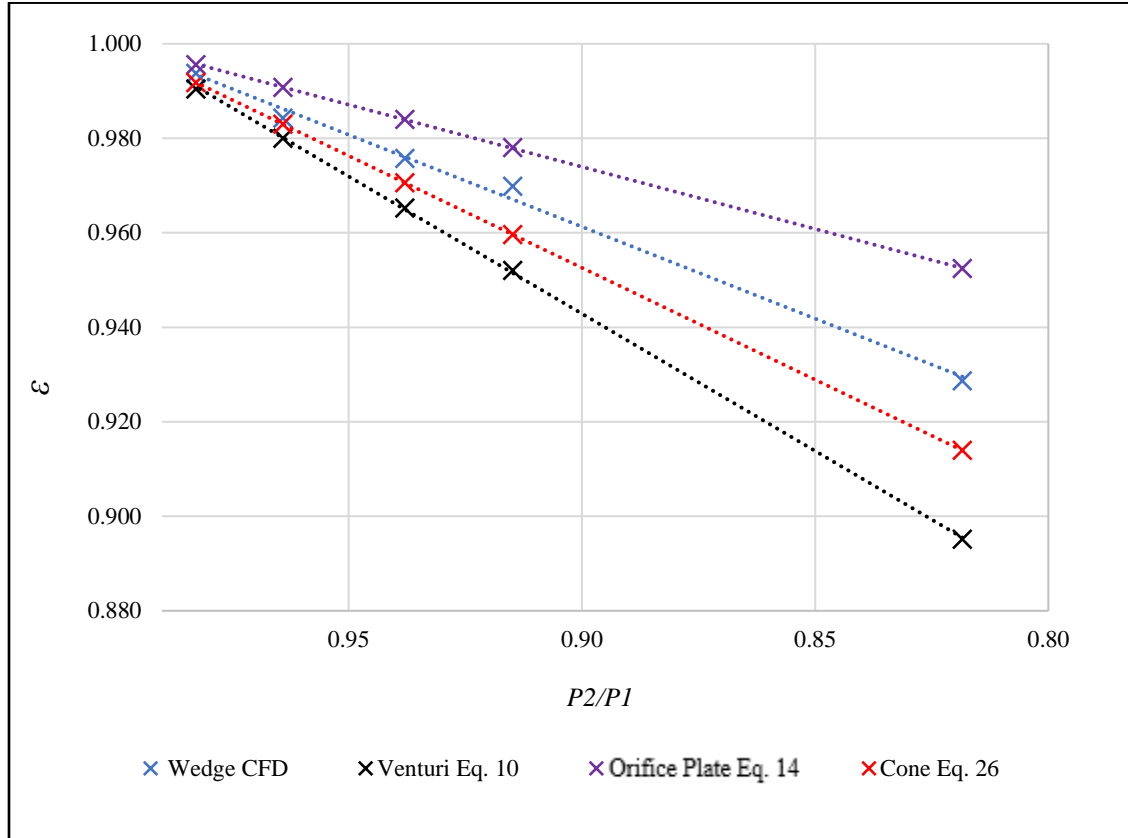


Figure 32. Gas Expansion Factors for A Variety of Differential Pressure Meters with  $\beta$  Values of 0.3789

### Compressible Flow Visualizations

This section is provided for readers interested in CFD visualizations of compressible flows' pressure, velocity, and density distributions through each DPFM geometry modeled in this study (Figures 33-41). Each DPFM presented in this section has a  $\beta$  value of approximately 0.5, a  $Re$  value of approximately 700,000, and an upstream tap pressure of approximately 0.11 MPa. Upon comparison of each DPFM's density scene, flow through the Classical Venturi experiences the smallest reduction in density and, therefore, the smallest expansion by an order of magnitude. Flow through the SC orifice plate

experiences the largest reduction in density and, therefore, the largest expansion. This is expected considering the magnitude of the pressure differential across each DPFM.

Interestingly, although flow through the Classical Venturi expands the least, for a given  $P_2/P_1$  value, the Classical Venturi has the lowest  $\varepsilon$  value and, therefore, experiences the largest reduction, relatively, in efficiency due to expansion when compared to SC orifice plates and wedge meters.

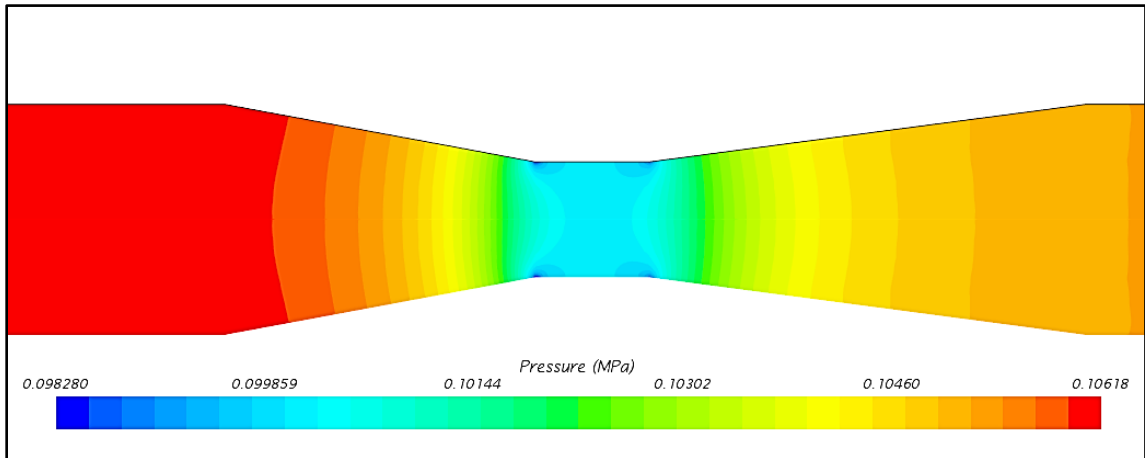


Figure 33. Classical Venturi Pressure Scene

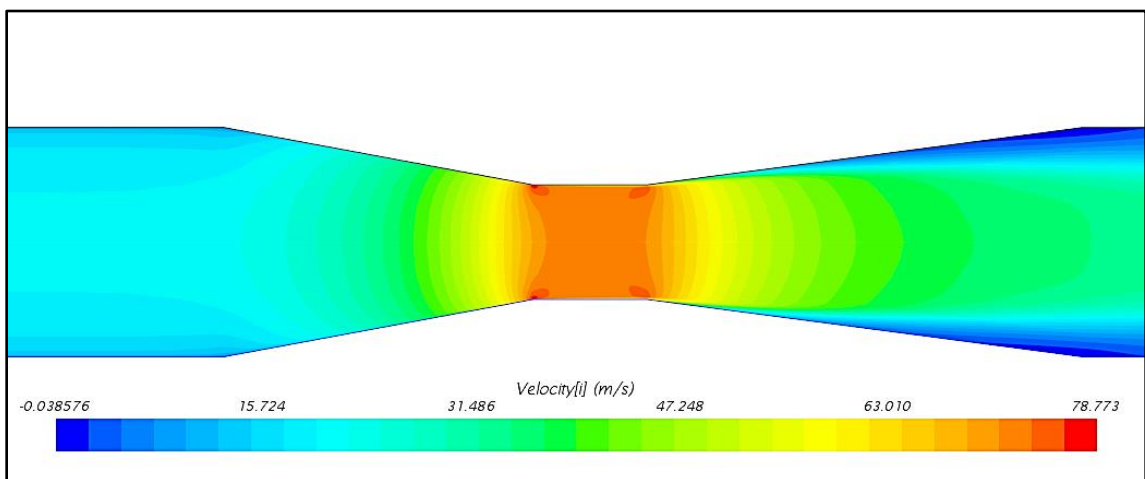


Figure 34. Classical Venturi Velocity Scene.

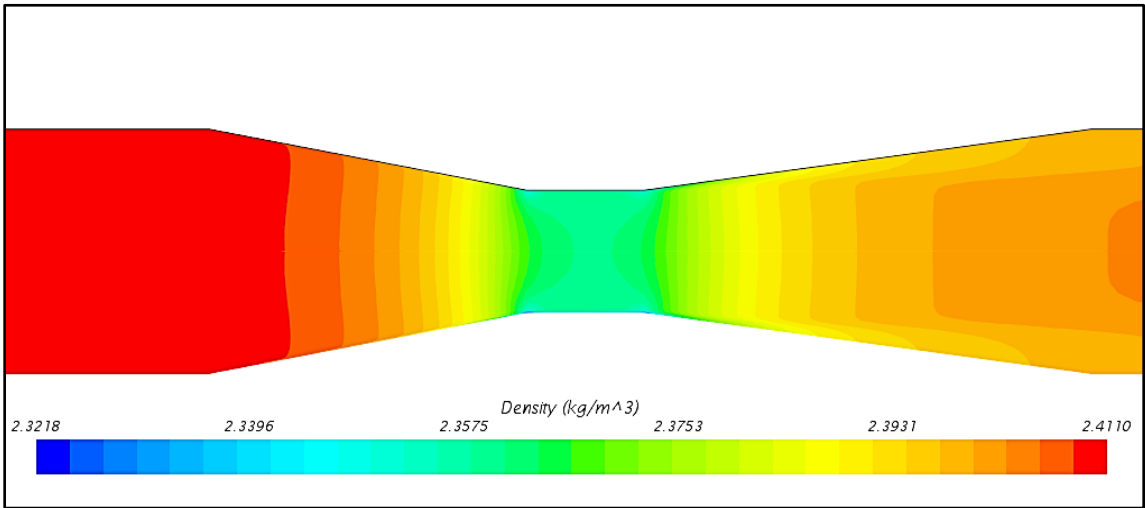


Figure 35 Classical Venturi Density Scene

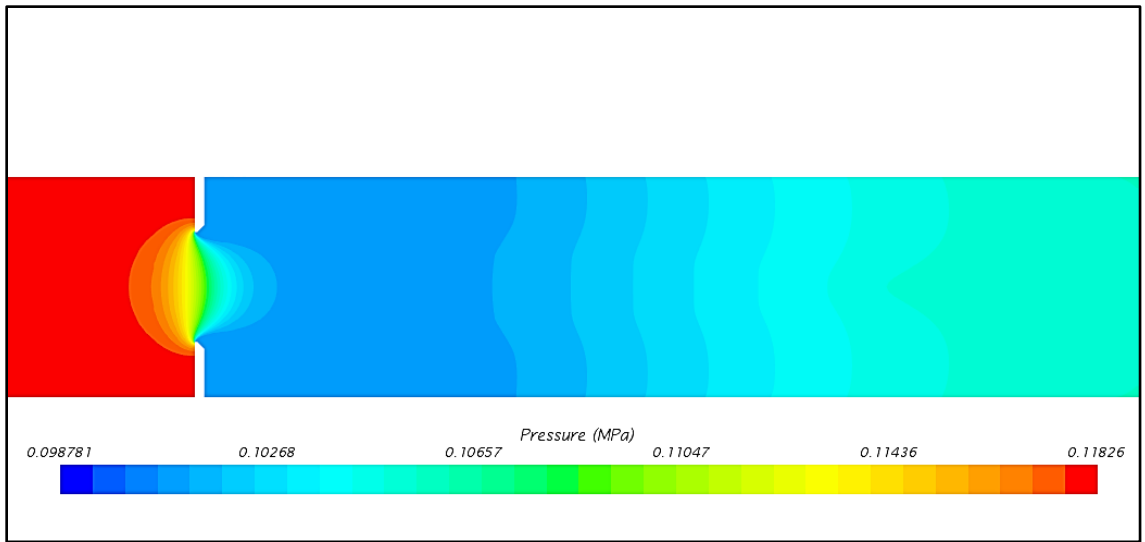


Figure 36. Standard Concentric Orifice Plate Pressure Scene

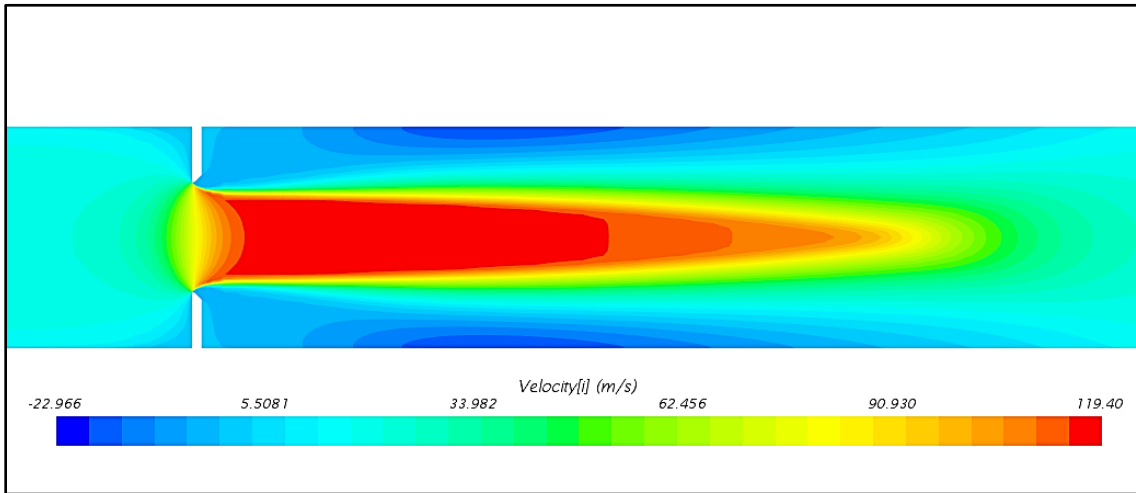


Figure 37. Standard Concentric Orifice Plate Velocity Scene

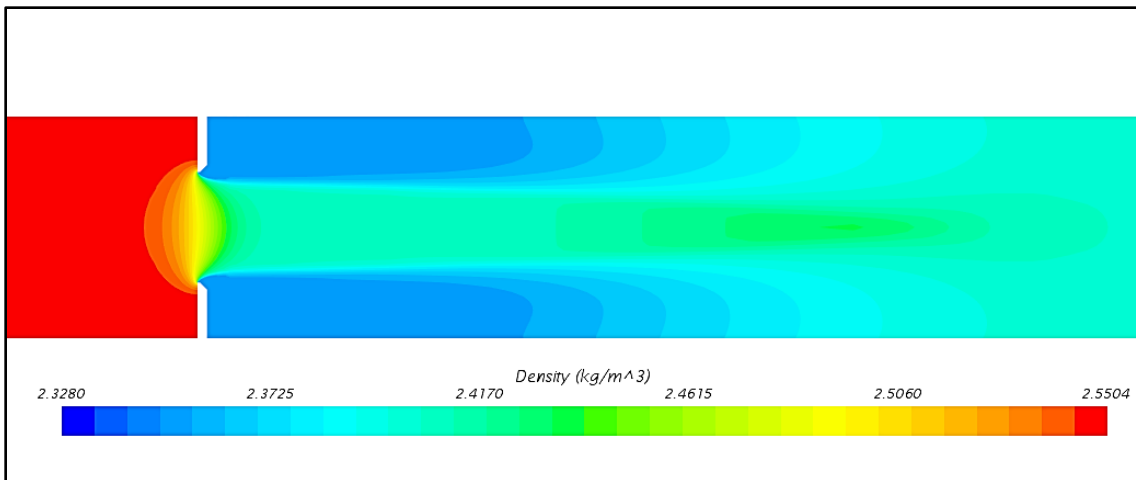


Figure 38. Standard Concentric Orifice Plate Density Scene

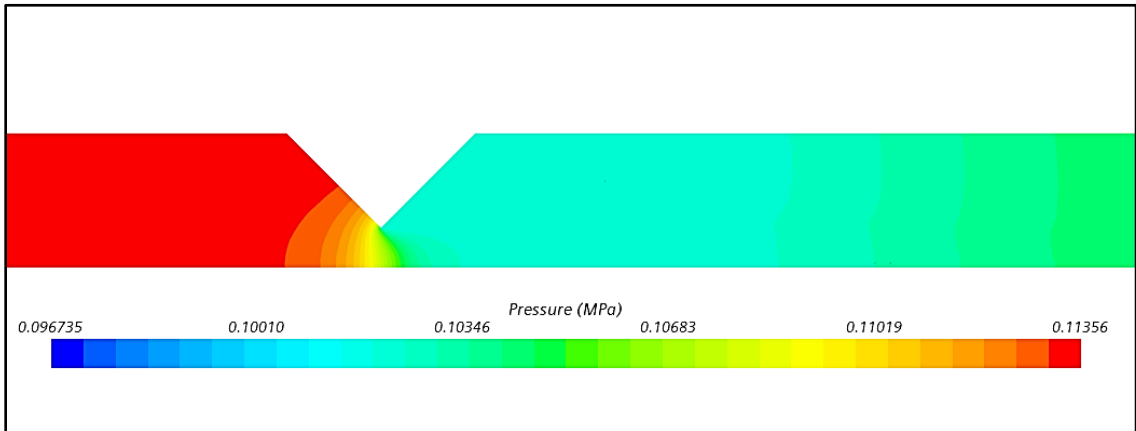


Figure 39. Wedge Meter Pressure Scene

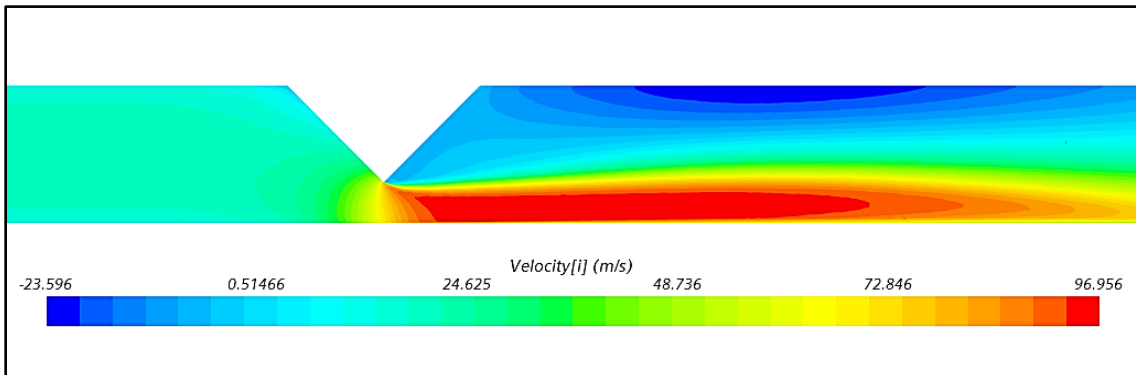


Figure 40. Wedge Meter Velocity Scene

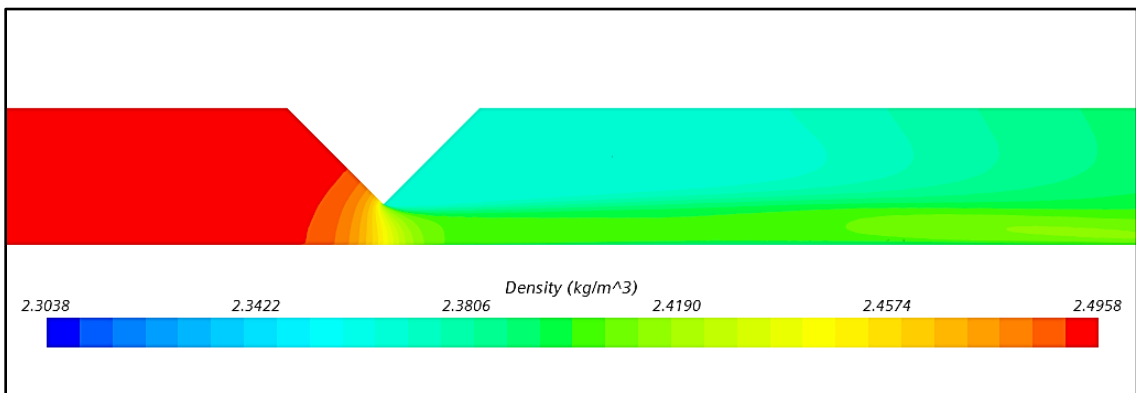


Figure 41. Wedge Meter Density Scene

### **Gas Expansion Factor to Mach Number Relationship**

The compressible flows simulated in this study were all restricted to subsonic velocities  $M \leq 0.7$ . In the range  $0.3 < M < 0.7$  the compressibility of the flow becomes more pronounced. Flows with  $M < 0.3$  are typically devoid of compressible behavior (Finnemore and Franzini 2002). Therefore,  $\varepsilon$  and  $M$  values were plotted for every DPFM and  $\beta$  value to better understand the relationship of  $\varepsilon$  and  $M$  of compressible flows in DPFMs (Figure 42). The  $M$  presented in this plot is the maximum  $M$  value occurring in an individual cell within a simulation's computation mesh. Interestingly, regardless of the DPFM geometry the relationship is approximately linear. This indicates plotting simulated  $\varepsilon$  values and  $M$  is a reasonable way to visually assess the validity of simulation results for DPFM geometries for which no laboratory  $\varepsilon$  data exists.

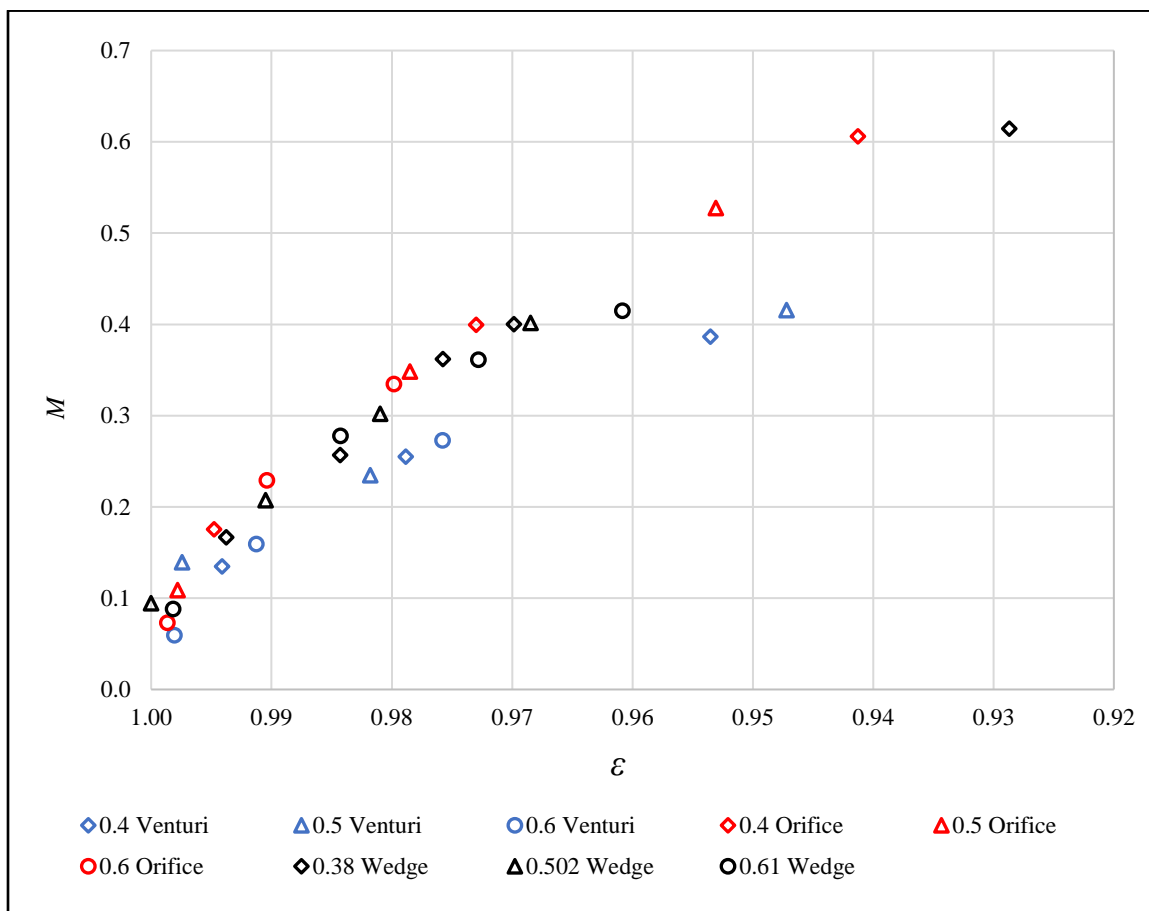


Figure 42. Gas Expansion Factor Mach Number Relationship

## CHAPTER VII

### CONCLUSION

There are many DPFM geometries for which empirical  $\varepsilon$  equations do not exist. Laboratory studies to determine  $\varepsilon$  values over a range of pressure differentials are extremely expensive to conduct. Therefore, the goal of this study was to investigate if relatively inexpensive CFD simulations can be used to predict  $\varepsilon$  values with sufficient accuracy for use in the regression of accurate empirical  $\varepsilon$  equations for a variety of DPFM geometries. More affordable generation of accurate empirical  $\varepsilon$  equations using CFD derived data would facilitate the application of new DPFM geometries for compressible flow metering, and potentially result in significant profits for the corresponding DPFMs' manufacture.

Simulations of incompressible and compressible flows through Classical Venturis, SC orifice plates, and wedge meters were conducted. Compressible flows were modeled using the assumption of a perfect gas with the fluid properties of dry air. Compressible effects were modeled using the ideal gas law equation of state. Classical Venturi and SC orifice plate CFD  $\varepsilon$  values matched their respective theoretical  $\varepsilon$  values with remarkable accuracy indicating CFD is an appropriate tool for determining  $\varepsilon$  values for DPFMs.

Wedge meter simulations were then conducted using the same modeling approach and reasonable  $\varepsilon$  values were predicted. Therefore, in conclusion this study's modeling approach can be used to determine reasonably accurate  $\varepsilon$  values for DPFM geometries as long as the assumption of perfect gas behavior is appropriate for compressible flow through the DPFM.

In addition, this study produced the following findings:

- $\varepsilon$  is relatively insensitive to the selected turbulence model.
- Comparing computed  $\varepsilon$  values against  $\varepsilon$  values calculated using Equations 10, 14, and 26 is a reasonable way to generally assess the validity of CFD derived  $\varepsilon$  data for which no laboratory  $\varepsilon$  data exists.
- The relationship between  $\varepsilon$  and  $M$  is approximately linear. Therefore, comparing CFD  $\varepsilon$  and  $M$  values is a reasonable way to estimate the validity of CFD derived  $\varepsilon$  data for which no laboratory  $\varepsilon$  data exists.

### **Future Research**

Based on the findings of this study, the following research topics should be investigated in future research:

- The impact of the working fluid (natural gas, nitrogen, steam) and, therefore, the isentropic exponent on CFD's ability to accurately predict  $\varepsilon$  values.
- The impact of pressure tap placement on the  $\varepsilon$  values of nonconcentric DPFMs.
- Using equations of state that better represent real gas behavior to model compressible flows, especially compressible flows with low temperatures and high pressures relative to the working fluids' critical temperature and pressure.
- A more comprehensive investigation of the impact turbulence model selection has on  $\varepsilon$  values for a variety of DPFM geometries.

- Modeling flows through other DPFM geometries to generate  $\varepsilon$  data that could be used to derive new empirical  $\varepsilon$  equations.

## REFERENCES

- ASME. (2007). Addenda to ASME MFC-3M-2004: measurement of fluid flow in pipes using orifice, nozzle, and venturi. *ASME MFC-3M-2004*, New York.
- ASME. (2008). Procedure for estimation and reporting of uncertainty due to discretization in CFD applications. *Journal of Fluids Engineering*, 130(7), 4.
- Banchhor, P. K., Singh, S. N., Seshardi, V., & Gandhi, B. K. (2004). Performance characteristics of wedge flowmeter using CFD. *Computation Fluid Dynamics Journal*, 11(3), 279-284.
- Buckingham E. (1932). Notes on the Orifice Meter: The Expansion Factor for Gases. *Bureau of Standards Journal of Research*. Research Paper No. 459. Vol.9. Washington. D.C.
- Finnemore, E. J., & Franzini, J. B. (2002). *Fluid mechanics with engineering applications*. Boston: McGraw-Hill.
- Halmi, D. (1973). Practical Guide to the Evaluation of the Metering Performance of Differential Producers. *Journal of Fluids Engineering*, 95(1), 127-141.  
doi:10.1115/1.3446945
- Hollingshead, C. L., Johnson, M. C., Dr, Barfuss, S. L., Dr, & Spall, R. E., Dr. (2011). Discharge coefficient performance of Venturi, standard concentric orifice plate,

V-cone, and wedge flow meters at low Reynolds numbers. *Journal of Petroleum Science and Engineering*, 78, 559-566.

ISO 5167-2:2003. (2003). Measurement of fluid flow by means of pressure differential devices inserted in circular cross-section conduits running full. – Part 2: Orifice plates.

ISO 5167-6:2019. (2019). Measurement of fluid flow by means of pressure differential devices inserted in circular cross-section conduits running full. – Part 6: Wedge Meters.

Kinghorn, F. C. (1986). The Expansibility Correction for Orifice Plates: EEC Data. *Proceedings of the Flow Measurement in the Mid 80's*. paper 5.2. East Kilbride, Scotland.

Kiš, R., Malcho, M., Janovcová, M. (2014). A CFD Analysis of Flow through a High-Pressure Natural Gas Pipeline with an Undeformed and Deformed Orifice Plate. *World Academy of Science, Engineering, and Technology International Journal of Mechanical and Mechatronics Engineering*, 8(3), 606-609.

LeTran, D. (2020). The Ideal Gas Law. *Libretexts*. Retrieved September 02, 2020.  
<[https://chem.libretexts.org/Bookshelves/Physical\\_and\\_Theoretical\\_Chemistry\\_Textbook\\_Maps/Supplemental\\_Modules\\_\(Physical\\_and\\_Theoretical\\_Chemistry\)/Physical\\_Properties\\_of\\_Matter/States\\_of\\_Matter/Properties\\_of\\_Gases/Gas\\_Laws/The\\_Ideal\\_Gas\\_Law](https://chem.libretexts.org/Bookshelves/Physical_and_Theoretical_Chemistry_Textbook_Maps/Supplemental_Modules_(Physical_and_Theoretical_Chemistry)/Physical_Properties_of_Matter/States_of_Matter/Properties_of_Gases/Gas_Laws/The_Ideal_Gas_Law)>

Miller, R. W. (1996). *Flow measurement engineering handbook* (3<sup>rd</sup> ed.). Boston, MA: McGraw-Hill.

Morrow, T. B. (2004), Metering Research Facility Program: Orifice Meter Expansion Factor Tests in 4-inch and 6-inch Meter Tubes. *Topical Report No GRI 04/0042*, Gas Technology Institute, Chicago, IL.

Morrow, T. B. (2004). Orifice Meter Expansion Factor Experiments. In *Proceedings of the 2004 ASME Heat Transfer/Fluids Engineering Summer Conference: Presented at 2004 ASME Heat Transfer/Fluids Engineering Summer Conference: July 11-15, 2004, Charlotte, North Carolina, USA* (Vol. 1, pp. 639-644). Charlotte, NC.

Murdock, J. W., & C. J. Foltz. (1953). Experimental Evaluation of Expansion Factors for Steam. *Transactions of the ASME*. 75 (5), 953-959.

Natural Gas Explained Use of Natural Gas. (2020, July 22). Retrieved September 2, 2020.

<<https://www.eia.gov/energyexplained/natural-gas/use-of-natural-gas.php>>

Prasanna, A., Seshadri, V., Dr, & Yogesh Kumar, K. J. (2016). Numerical Analysis of Compressible Effect in the Flow Metering By Classical Venturimeter. *International Journal of Engineering Sciences & Research Technology*, 5(6), 603-616.

- Prassanna, A., Seshadri, V., Dr., & Yogesh Kumar, K. J. (2016). Analysis of Compressible Effect in the Flow Metering BY Orifice Plate Using CFD. *International Journal of Scientific Research, in Science, Engineering, and Technology*. 2(4), 170-180.
- Reader-Harris, M. (1998). “The Equation for the Expansibility Factor for Orifice Plates” FLOMEKO 1998. Lund, Sweden, June 1998. –P. 209–214.
- Seidl W. (1995). The orifice expansion correction for a 50 mm line size at various diameter ratios. *Proceedings of the 3rd international fluid flow measurement symposium*. San Antonio, TX.
- Sharp, Z. B. (2016). Applications of computational fluid dynamics in flow measurement and meter design. Ph.D. Dissertation. Utah State University. Logan, UT.
- Siemens. (2020). Reynolds-Averaged Navier-Stokes (RANS) Turbulence Models. <[https://documentation.thesteveportal.plm.automation.siemens.com/starccmplus\\_1atest\\_en/index.html#page/STARCCMP%2FGUID-7237C585-2707-4FCC-BB3FE2376C68B114.html](https://documentation.thesteveportal.plm.automation.siemens.com/starccmplus_1atest_en/index.html#page/STARCCMP%2FGUID-7237C585-2707-4FCC-BB3FE2376C68B114.html)>
- Stewart, D., Reader-Harris, M. J., & Peters, R. J. W. (2001). Derivation of an expansibility factor for the V-Cone meter. Flow Measurement 2001 International Conference.

United States Natural Gas Industrial Price. (2020, August 31). Retrieved September 2, 2020.

<<https://www.eia.gov/dnav/ng/hist/n3035us3A.html>>

Versteeg, H. K., & Malalasekera, W. (2011). *An introduction to computational fluid dynamics: The finite volume method*. Harlow: Pearson Education.

## Appendix

## Grid Convergence Index Results

“Procedure for estimation and reporting of uncertainty due to discretization in CFD applications” recommends reporting the GCI study values of  $p$ ,  $e_a^{21}$ ,  $e_{ext}^{21}$ ,  $GCI_{fine}^{21}$  as well as the occurrence of negative  $S$  values which are indicative of oscillatory convergence. These GCI study results are present in tabulated form for each DPFM geometry and incompressible or compressible flow (Tables A1-A6). Note in the following tables:

- $Re_{avg}$  is the average  $Re$  values of the three simulations used determine one set of GCI values (i.e. one row in each table).
- $C_d$  is the incompressible or compressible discharge coefficient depending on the fluid type.
- $S$  values of -1 indicate oscillatory convergence.
- The column “Model Space” is included for the Classical Venturi GCI table because both axisymmetric and three-dimensional simulations were conducted for this DPFM geometry

Table A1. Classical Venturi GCI Study Results

$\beta$	Fluid	Model Space	$R_{e_{avg}}$	$C_{d_1}$	$C_{d_2}$	$C_{d_3}$	$p$	$e_a^{21}$	$e_{ext}^{21}$	$GCI_{fine}^{21}$	$S$
0.4	Water	Axis	616827	0.98680	0.98606	0.98585	3.64	0.0751%	0.0296%	0.0371%	1
0.4	Air	Axis	606231	0.94054	0.94024	0.94007	1.48	0.0313%	0.0465%	0.0582%	1
0.5	Water	Axis	599434	0.98546	0.98528	0.98496	1.57	0.0185%	0.0257%	0.0321%	1
0.5	Air	Axis	601926	0.96804	0.96808	0.96809	6.59	0.0047%	0.0005%	0.0007%	1
0.5	Water	3D	600669	0.98618	0.98563	0.98554	5.26	0.0560%	0.0108%	0.0135%	1
0.5	Air	3D	602634	0.96789	0.96786	0.96784	0.43	0.0028%	0.0173%	0.0216%	1
0.6	Water	Axis	1497187	0.98763	0.98748	0.98697	3.35	0.0160%	0.0073%	0.0091%	1
0.6	Air	Axis	1504367	0.96423	0.96399	0.96341	2.53	0.0251%	0.0179%	0.0224%	1

Table A2. Standard Concentric Orifice Plate GCI Study Results

$\beta$	Fluid	$R_{e_{avg}}$	$C_{d_1}$	$C_{d_2}$	$C_{d_3}$	$p$	$e_a^{21}$	$e_{ext}^{21}$	$GCI_{fine}^{21}$	$S$
0.4	Water	701504	0.60087	0.60159	0.60255	0.83	0.1199%	0.3595%	0.4478%	1
0.4	Air	855233	0.56540	0.56609	0.56549	0.38	0.1219%	0.8659%	1.0731%	-1
0.5	Water	1151362	0.60446	0.60528	0.60481	1.60	0.1370%	0.1858%	0.2318%	-1
0.5	Air	1140392	0.57615	0.57688	0.57722	2.28	0.1276%	0.1063%	0.1328%	1
0.6	Water	1151620	0.60942	0.60951	0.60929	2.09	0.0141%	0.0043%	0.0054%	-1
0.6	Air	1044844	0.59761	0.59801	0.59811	4.35	0.0684%	0.0194%	0.0243%	1

Table A3. Wedge GCI Study Results

$\beta$	Fluid	$R_{e_{avg}}$	$C_{d_1}$	$C_{d_2}$	$C_{d_3}$	$p$	$e_a^{21}$	$e_{ext}^{21}$	$GCI_{fine}^{21}$	$S$
0.3789	Water	1102109	0.74206	0.74177	0.74764	8.66	0.0394%	0.0394%	0.0026%	-1
0.3789	Air	339483	0.73146	0.73203	0.73967	7.50	0.0777%	0.0062%	0.0078%	1
0.5019	Water	1102106	0.72947	0.73055	0.73256	1.80	0.1476%	0.1705%	0.2128%	1
0.5019	Air	959087	0.70653	0.70718	0.70951	3.72	0.0910%	0.0345%	0.0432%	1
0.6107	Water	1499918	0.71790	0.71790	0.71790	3.27	0.1446%	0.0687%	0.0858%	1
0.6107	Air	921144	0.70414	0.70485	0.70643	2.30	0.1011%	0.0831%	0.0831%	1